Stability of asynchronous variational integrators

William Fong [a], Eric Darve [a,b,*], Adrian Lew [a,b]

[a] Institute for Computational and Mathematical Engineering, Stanford University, USA
[b] Department of Mechanical Engineering, Stanford University, USA

ABSTRACT

The adoption of multiple time step integrators can provide substantial computational savings for mechanical systems with multiple time scales. However, the scope of these savings may be limited by the range of allowable time step choices. In this paper we analyze the linear stability of the fully asynchronous methods termed AVI, for asynchronous variational integrators. We perform a detailed analysis for the case of a one-dimensional particle moving under the action of a soft and a stiff quadratic potential, integrated with two time steps in rational ratios. In this case, we provide sufficient conditions for the stability of the method. These generalize to the fully asynchronous AVI case the results obtained for synchronous multiple time stepping schemes, such as r-RESPA, which show resonances when the larger time step is a multiple of the effective half-period of the stiff potential. Additionally, we numerically investigate the appearance of instabilities. Based on the experimental observations, we conjecture the existence of a dense set of unstable time steps when arbitrary rational ratios of time steps are considered. In this way, unstable schemes for arbitrarily small time steps can be obtained. However, the vast majority of these instabilities are extremely weak and do not present an obstacle to the use of these integrators. We then applied these results to analyze the stability of multiple time step integrators in the more complex mechanical systems arising in molecular dynamics and solid dynamics. We explained why strong resonances are ubiquitously found in the former, while rarely encountered in the latter. Finally, in this paper we introduce a formulation of AVI that highlights the symplectic nature of the algorithm, complementing those introduced earlier by other authors.

1. Introduction

Symplectic integrators are usually adopted as the integrators of choice for molecular dynamics simulation of systems of particles (bio-molecules, proteins, crystals...) and for some computational mechanics applications. One of the reasons behind this choice is their excellent long-time energy conservation properties, which can be traced back to the existence of a shadow Hamiltonian function almost exactly conserved by the numerical trajectory, see, e.g. [40,5].

A powerful and flexible approach for deriving symplectic integrators stems from a discrete version of Hamilton's principle, which led to the development of variational integrators [46,30,33,27]. In this approach the starting point consists in constructing a suitable approximation to the action integral, termed the action sum. The algorithm then follows by requesting

* Corresponding author. Address: Department of Mechanical Engineering, Stanford University, Durand 209, 496 Lomita Mall, Stanford, CA 94305-4040, USA.
E-mail addresses: willfong@stanford.edu (W. Fong), darve@stanford.edu (E. Darve), lewa@stanford.edu (A. Lew).

the discrete trajectory to be a stationary point of the action sum. Any variational integrator is symplectic, and conversely. Additionally, variational integrators can be constructed to have other outstanding conservation properties by taking advantage of a discrete version of Noether's theorem [29,33,28], which guarantees that for each symmetry operation of the discrete action there exists a corresponding conserved quantity, as in the continuous-time case. These and other features of the theory of variational integrators have been thoroughly discussed in many earlier references (see previous references and [49,32,48,36,27,33]); hence we shall skip further discussions herein.

Asynchronous variational integrators (AVI) are a class of variational integrators distinguished by the trait of enabling the use of different time steps for different potential energy contributions to a mechanical system. Their formulation and use in the context of finite-element (FE) discretizations in solids and some fluid mechanics simulations can be found in [26–28], and they essentially amount to considering a possibly-different time step for each element in the mesh. These algorithms share many features with other multiple time step methods in computational mechanics, commonly known as subcycling or element-by-element methods [37,4,4,37,21,45,10,8,7,13,12].

In the context of molecular dynamics, r-RESPA [47,14] is perhaps the most widely known multiple time step method. It has been long recognized that this method can display resonance instabilities, especially in the context of molecular dynamics simulations [22,1,41,43,31,6]. These resonances severely limit the relative size of the time steps. Several approaches have been proposed to reduce these instabilities. Schlick et al. [1,2,39] used Langevin dynamics along with extrapolative methods. An appropriate choice of the friction coefficient in the Langevin equation stabilizes the trajectories even with very large time steps. The isokinetic Nosé-Hoover chain RESPA proposed by Minary et al. [35] is another method that produces stable trajectories for large time steps. Mollified versions of r-RESPA such as MOLLY were developed by Izaguirre et al. [23]. MOLLY retains instabilities but they appear for larger values of the time steps (up to 50% greater). When the fast potentials are assumed to be quadratic, an elegant procedure, called the two-force method [16,17], removes all resonances and captures the correct coupling between slow and fast forces (see also [19]). However, the extension of this scheme to situations with more than two time steps has not been reported so far.

Contrary to molecular dynamics, resonance instabilities have not hampered the use of multiple time step methods in computational solid mechanics. Stability analyses for several subcycling methods have been performed [20,3,9,8,7]. In particular, many interesting aspects of the stability of some subcycling methods have been highlighted in [8,9]. Therein, it was posited that the reason behind the successful performance of multiple time step methods in solid dynamics is that the set of resonant time steps is very small. Consequently (within some reasonable stability considerations), it is unlikely in practice that resonant time steps will be chosen. Even though the algorithms analyzed therein are not symplectic, and hence essentially differ from AVI, we shall see that these same observations are valid for AVI.

The key distinctive feature of AVI over r-RESPA or many of the subcycling algorithms is that time steps in arbitrary ratios can be considered. This extra degree of freedom becomes very useful in FE simulations, since time steps can be made to vary smoothly throughout the mesh. In the molecular dynamics context, this freedom enables the adoption of more general decompositions of the potential energy, each one with a characteristic time and length scale. In fact, as we shall discuss in this document, AVI generalizes r-RESPA to arbitrary (instead of integer) time step ratios.

The complex stability considerations found in previous multiple time step methods with integer time step ratios is enriched when rational time step ratios are considered. The description of these novel features and their analysis are one of the two main contributions of this document. The second key contribution is to utilize this analysis and some carefully crafted numerical experiments to explain the dichotomy in the behavior of AVI between molecular and solid dynamics simulations.

The key contributions of the paper are:

  (i) A linear stability analysis of AVI when two time steps h_1 and h_2 are used to integrate a one-degree of freedom harmonic oscillator whose potential energy has been split into a stiff and a soft part. We provide, in the form of Proposition 1, a bound on the trace of the amplification matrix for integrators in which h_2/h_1 is a rational number. As a corollary, a sufficient condition for the stability of the integrator follows. The resulting possible unstable time step combinations generalize those obtained for r-RESPA in [1,39] for the same system.

 (ii) A conjecture that the set of unstable time steps is dense and that arbitrary small unstable time steps exist. This conjecture is suggested by the theoretical analysis and numerical experiments. Systematic numerical tests in which all unstable time steps were obtained along lines of the form $h_2 = (p/q)h_1$ (p and q integers) strongly support this conjecture. Most of these resonances, however, are extremely weak and would require millions of time steps or more to be observed, so they have no practical implications.

(iii) A numerical study of the location of the strongest instabilities as a function of h_1 and h_2, again for a harmonic oscillator, which is similar to that presented in [11]. We propose a criterion to characterize the location of the strongest resonances, and verify its validity by predicting the location of the most important resonances in the h_1-h_2 plane.

(iv) We demonstrate, through numerical examples and some analysis, that the weak long-range forces often present in molecular dynamics are the key culprit for the stringent stability limitations of AVI. In the context of solid dynamics, the local coupling between elements leads to a weak coupling between stiff and soft regions when these vary smoothly in space. We show that as a consequence the set of time steps leading to unstable schemes is very small, explaining why these resonance instabilities that are pervasive in molecular dynamics are only seldom observed in FE simulations with AVI.

Perhaps surprisingly, most of the features in the molecular dynamics and solid mechanics examples can be simply understood with the analysis of the one-degree of freedom system. The integration of weak long-range forces with a large time step near an integer multiple of the half-period of one of the natural modes in the system leads to a resonance instability. This is manifested as an exponential growth of the amplitude of that mode. The width of the resonance for each mode, i.e. the range of time steps for which a resonance is encountered, decreases with the stiffness of the long-range forces. Consequently, the weaker the forces the more difficult it is to excite a resonant mode, and the slower the exponential growth is. In molecular dynamics, the fact that long-range forces interact with every single degree of freedom in the molecule leads to wide resonance intervals. Since in large molecular systems the set of natural frequencies is dense, it is almost certain that beyond a certain threshold one of these frequencies will satisfy the resonance condition. The same limitation is found in most other methods such as r-RESPA.

In contrast, in solid dynamics, soft elements integrated with large time steps also have the possibility of inducing a resonance in one or more of the high-frequency or stiff natural modes of the discrete structure. However, numerical examples and analytical considerations show that the amplitude of the stiff modes decays exponentially fast in a soft region; this leads to a very weak coupling between stiff and soft elements and to very narrow resonance intervals. These resonances are so difficult to encounter even when an explicit effort to find them is made, that they effectively have no practical implications, leading to a robust multiple time step integration algorithm. For the same reasons, it follows that it is safer to pick time steps which vary smoothly in space, so that sudden transitions from stiff to soft materials do not induce resonant instabilities. This is consistent with the findings in [9] for other multiple time step integrators in solid dynamics.

This paper is organized as follows: in Section 2 we present the derivation of AVI from a discrete version of Hamilton's principle, and comment about its implementation. Although the algorithm is essentially identical to that introduced in [27], it is presented here in a framework better suited for molecular dynamics applications. The key difference is the definition of the positions for *all* the degrees of freedom at every potential update. This enables the construction of a single discrete Lagrangian between any two consecutive potential updates, as opposed to the discrete Lagrangians per element that naturally appear in the continuum mechanics setting of [27], but that do not have a natural analog in the ordinary differential equation case. By construction, it is then evident that AVI is symplectic. The AVI algorithm is presented in the non-staggered form which is commonly found in molecular dynamics integrators.

In Section 3, the stability of r-RESPA discretizations for a harmonic oscillator is reviewed [1,39], since it is essential for the subsequent analysis of the more complex AVI case in Section 4. Therein, the analysis proceeds by studying the stability behavior of AVI in the case of a harmonic oscillator formed by two springs, in which one is very soft relative to the other. The analysis reveals a sufficient condition for stability. We are not able to specify the behavior of the discretization when these conditions are not satisfied, but numerical experiments show that instabilities are systematically encountered in at least part of each connected time step interval in which these conditions are not met. A study of our conjecture that the set of unstable time steps is dense follows. In particular, we provide specific examples of extremely small time steps which lead to an exponential growth of the energy. The study of the location of the strongest resonances for the harmonic oscillator is also presented here.

Section 5 contains the study of resonance instabilities for AVI in molecular dynamics and solid dynamics simulations. Conclusions are provided in Section 6.

2. Variational derivation of AVI

To review the main ideas behind variational integrators we begin by recalling the simple case of the velocity Verlet (VV) integrator and by showing its variational nature. This will simplify the later introduction of AVI. Consider a system of N particles with masses $m = (m_1, \ldots, m_N)$, and positions given by Cartesian coordinates $x = (x_1, \ldots, x_N)$ with corresponding velocities $v = \dot{x} = (v_1, \ldots, v_N)$; these particles interact according to a given potential function $V(x)$. Their trajectories $x(t)$ are governed by Newton's equations of motion $F = \mathbf{M}a$ where $F = -\nabla V(x)$, $\mathbf{M}$ is the diagonal matrix with the particle masses along the diagonal, and $a = \ddot{x}$. For this system the VV integrator is given by:

$$v^{j+1/2} = v^j + \frac{h}{2}\mathbf{M}^{-1}F^j, \tag{1a}$$

$$x^{j+1} = x^j + hv^{j+1/2}, \tag{1b}$$

$$v^{j+1} = v^{j+1/2} + \frac{h}{2}\mathbf{M}^{-1}F^{j+1}, \tag{1c}$$

where h is the time step, $t^j = jh$, $x^j = x(t^j)$, $v^j = v(t^j)$, and $F^j = F(x^j)$, for any non-negative integer j. The VV integrator can also be written in a time-staggered form:

$$x^{j+1} = x^j + hv^{j+1/2},$$

$$v^{j+3/2} = v^{j+1/2} + h\mathbf{M}^{-1}F^{j+1}.$$

The VV integrator is commonly used in molecular dynamics because it is easy to implement, has a low computational cost, and conserves energy remarkably well.

We next review the variational derivation of the VV integrator, as shown for example in [24]. Following the usual convention in Lagrangian mechanics, the position x and velocity v will be denoted by q and $\dot{q}$, respectively. The Lagrangian for the system defined above is given by the difference between the kinetic and potential energies:

$$L(q,\dot{q}) = \sum_{a=1}^{N} \frac{1}{2} m_a \|\dot{q}_a\|^2 - V(q),$$

where m_a is the mass of particle a and $\dot{q}_a$ is the velocity of particle a. The action of an arbitrary trajectory $q(t)$ of the Lagrangian system is defined as the time integral of $L(q(t),\dot{q}(t))$ in the interval of interest $[0,T]$:

$$S[q(\cdot)] = \int_0^T L(q(t),\dot{q}(t))\mathrm{d}t.$$

Hamilton's variational principle states that the trajectory $q(t)$ followed by the particles is a stationary point of the action integral S among all smooth trajectories with the same initial and end points, $q(0)$ and $q(T)$, respectively. The Euler–Lagrange equations of this variational principle are precisely Newton's equations of motion.

Variational integrators are constructed by mimicking this variational structure in the discrete case. The essential idea is to approximate the action over a discrete trajectory and use a discrete variational principle to obtain the algorithm. More precisely, the time interval $[0,T]$ is partitioned into a sequence of times $\{t^j\} = \{t^0 = 0,\ldots,t^M = T\}$ with a time step h, and a discrete trajectory on this partition is a sequence of positions $\{q^j\} = \{q^0,\ldots,q^M\}$. The approximation of the action, the action sum, is constructed as

$$S_\mathrm{d}[\{q^j\}] = \sum_{i=0}^{M-1} L_\mathrm{d}(q^i, q^{i+1}),$$

where $L_\mathrm{d}(q,\tilde{q})$ is the discrete Lagrangian, which in the case of VV takes the form:

$$L_\mathrm{d}(q,\tilde{q}) = h\left(\sum_{a=1}^{N} \frac{1}{2} m_a \left\|\frac{\tilde{q}_a - q_a}{h}\right\|^2 - \frac{V(q) + V(\tilde{q})}{2}\right). \tag{2}$$

The integrator follows by employing a discrete version of Hamilton's principle: the discrete trajectory renders $\delta S_\mathrm{d} = 0$ for any variation δq satisfying $\delta q^0 = 0$ and $\delta q^M = 0$. The discrete Euler–Lagrange equations for this variational principle are

$$D_1 L_\mathrm{d}(q^j, q^{j+1}) + D_2 L_\mathrm{d}(q^{j-1}, q^j) = 0 \tag{3}$$

for $j = 1,\ldots,M-1$, where $D_i L_\mathrm{d}(\cdot,\cdot)$ indicates the partial derivative of L_d with respect to its ith argument. This equation implicitly defines a map $(q^{j-1}, q^j) \mapsto (q^j, q^{j+1})$, which is the algorithm. The momenta $\{p^j\}$ are generally defined to be

$$p^j = D_2 L_\mathrm{d}(q^{j-1}, q^j) = -D_1 L_\mathrm{d}(q^j, q^{j+1}), \tag{4}$$

where the second equality follows from the discrete Euler–Lagrange equations (3). For the discrete Lagrangian (2) and Eq. (4), the momenta are given by

$$p_a^j = m_a\left(\frac{q_a^j - q_a^{j-1}}{h}\right) - \frac{h}{2}\frac{\partial V}{\partial q_a}(q_a^j) = m_a\left(\frac{q_a^{j+1} - q_a^j}{h}\right) + \frac{h}{2}\frac{\partial V}{\partial q_a}(q_a^j). \tag{5}$$

Eqs. (1a)–(1c) are recovered provided the velocities at half steps are defined as

$$\dot{q}^{j+1/2} = \frac{q^{j+1} - q^j}{h}.$$

Eq. (4) implicitly defines a symplectic map $(q^j, p^j) \mapsto (q^{j+1}, p^{j+1})$, see e.g. [17], so that all variational integrators are symplectic. In the case of VV, from Eq. (5) and given (q^j, p^j):

$$p_a^j = m_a\left(\frac{q_a^{j+1} - q_a^j}{h}\right) + \frac{h}{2}\frac{\partial V}{\partial q_a}(q_a^j) \Rightarrow q_a^{j+1} = q_a^j + \frac{h}{m_a}\left(p_a^j - \frac{h}{2}\frac{\partial V}{\partial q_a}(q_a^j)\right),$$

$$p_a^{j+1} = m_a\left(\frac{q_a^{j+1} - q_a^j}{h}\right) - \frac{h}{2}\frac{\partial V}{\partial q_a}(q_a^{j+1}).$$

As a result, variational integrators conserve energy very well (no drift) over long-time scales [38,15]. This is a key property for molecular dynamics and other problems.

We discuss next the derivation of AVI. The types of asynchronous discretizations discussed herein are applicable to situations in which the potential $V(q)$ can be written as the sum of K potentials:

$$V(q) = \sum_{k=1}^{K} V_k(q).$$

In the context of finite-element discretizations of continuum mechanics equations this decomposition is naturally accomplished on an element-by-element basis, while in the context of molecular dynamics for large proteins it is often achieved by splitting the forces into strong, short-ranged ones and weak, long-ranged ones. In these situations it is possible to integrate each one of the potentials V_k with a different time step, obtaining in this way a more efficient algorithm for a given desired accuracy.

The idea is then to assign to each potential V_k a sequence of times $\{0 = t_k^0 < \cdots < t_k^{M_k} = T\}$. Additionally, we construct the sequence of all times in the system $\{\theta^0 < \theta^1 < \cdots < \theta^M\}$ by lumping together all potential times in a strictly increasing sequence; see the example in Fig. 1. As before, the position of the system at time θ^i is denoted by q^i, and a discrete trajectory is the sequence of positions $\{q^0, \ldots, q^M\}$. For each time θ^i we define the set $\mathscr{K}(i)$ as

$$\mathscr{K}(i) = \{k | \exists j, t_k^j = \theta^i\}.$$

For each $k \in \mathscr{K}(i)$, we can define:

$$h_k^{i+1/2} \stackrel{\text{def}}{=} t_k^{j+1} - t_k^j \quad \text{and} \quad h_k^{i-1/2} \stackrel{\text{def}}{=} t_k^j - t_k^{j-1},$$

where $t_k^j = \theta^i$.

The discrete Lagrangian for AVI is

$$L_d(q, \tilde{q}, i) = \sum_{a=1}^N \frac{1}{2} m_a \Delta\theta \left\| \frac{\tilde{q}_a - q_a}{\Delta\theta} \right\|^2 - \sum_{k \in \mathscr{K}(i)} \frac{h_k^{i+1/2}}{2} V_k(q) - \sum_{k \in \mathscr{K}(i+1)} \frac{h_k^{i+1/2}}{2} V_k(\tilde{q}) \tag{6}$$

with $\Delta\theta = \theta^{i+1} - \theta^i$. The discrete action sum follows as

$$S_d = \sum_{i=0}^{M-1} L_d(q^i, q^{i+1}, i).$$

A graphical interpretation of this discrete Lagrangian is shown in Fig. 2.

One of the noteworthy features of this presentation, in contrast to that in [27], is that the discrete Lagrangian is not a consistent approximation of the action during a time interval (θ^i, θ^{i+1}), in the sense explained in [33]. Nonetheless, S_d is still a consistent approximation of the action over the whole trajectory during the time interval $[0, T]$. This is evident from rearranging the terms in the sum, namely

$$S_d = \sum_{a=1}^N \sum_{i=0}^{M-1} \frac{1}{2} m_a (\theta^{i+1} - \theta^i) \left\| \frac{q_a^{i+1} - q_a^i}{\theta^{i+1} - \theta^i} \right\|^2 - \sum_{k=1}^K \sum_{j=0}^{M_k-1} (t_k^{j+1} - t_k^j) \frac{V_k(q^{kj+1}) + V_k(q^{kj})}{2},$$
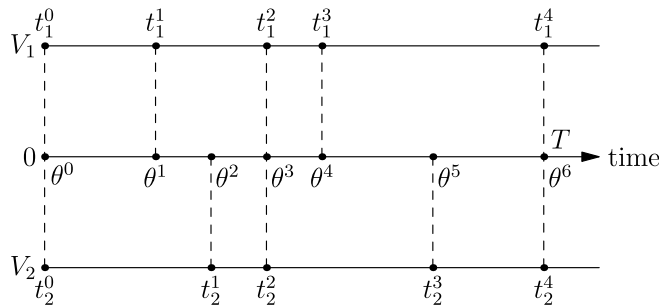
where q^{kj} is the position at time t_k^j. The discrete Euler–Lagrange equations take the form:

$$m_a \dot{q}_a^{i+1/2} - m_a \dot{q}_a^{i-1/2} = - \sum_{k \in \mathscr{K}(i)} \frac{h_k^{i-1/2} + h_k^{i+1/2}}{2} \frac{\partial V_k}{\partial q_a}(q^i), \tag{7}$$

where

$$\dot{q}_a^{i+1/2} \stackrel{\text{def}}{=} \frac{q_a^{i+1} - q_a^i}{\theta^{i+1} - \theta^i}.$$

Eq. (4) defines the momenta $\{p^0, \ldots, p^M\}$, to wit

Fig. 1. Example of a time discretization for AVI. In this case a split into two potential energy functions is adopted. The times for potential V_1 are $\{0, t_1^1, t_1^2, t_1^3, t_1^4\}$ and those of potential V_2 are $\{0, t_2^1, t_2^2, t_2^3, t_2^4\}$. The resulting set of all time steps in the system is $\{\theta^0 = t_1^0 = t_2^0, \theta^1 = t_1^1, \theta^2 = t_2^1, \theta^3 = t_1^2 = t_2^2, \theta^4 = t_1^3, \theta^5 = t_2^3, \theta^6 = t_1^4 = t_2^4 = T\}$.
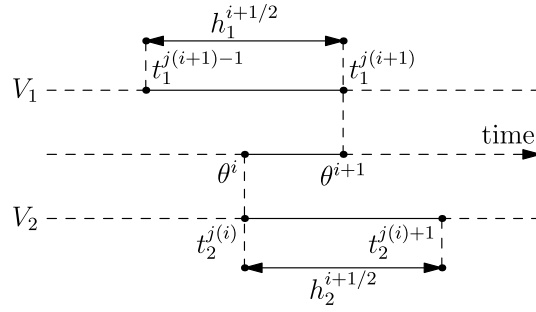
Fig. 2. Graphical interpretation of the arguments of the discrete Lagrangian for AVI, Eq. (6), for a generic time interval (θ^i, θ^{i+1}). The first term on the right-hand side of Eq. (6) approximates the action stemming from the kinetic energy during (θ^i, θ^{i+1}). In contrast, each one of the two remaining terms account for one half of the contribution of potentials at time θ^i and θ^{i+1}.

$$p_a^i = m_a \dot{q}_a^{i-1/2} - \sum_{k \in \mathscr{K}(i)} \frac{h_k^{i-1/2}}{2} \frac{\partial V_k}{\partial q_a}(q^i) = m_a \dot{q}_a^{i+1/2} + \sum_{k \in \mathscr{K}(i)} \frac{h_k^{i+1/2}}{2} \frac{\partial V_k}{\partial q_a}(q^i).$$

This derivation of AVI and the method itself differ slightly from those provided in [27,28]. The first difference with [27,28] is the precise definition of the map $(q^i, p^i) \mapsto (q^{i+1}, p^{i+1})$, which was absent in the previous references. One key consequence is that it makes the symplectic nature of the asynchronous discretization evident: due to the two-point discrete Lagrangian in Eq. (6) and its associated definition of the momenta, the resulting map is symplectic. In contrast, in [27], it is shown that AVI is a multi-symplectic algorithm, which is a natural concept in the context of continuum mechanics, but that lacks a clear or traditional interpretation in the ordinary differential equations setting.

The second difference is the use of a trapezoidal rule to approximate the action integral within each elemental time step, as opposed to the rectangle rule adopted in [27,28]. A consequence of this choice is the appearance of the average of two consecutive time step sizes in the discrete Euler–Lagrange equations (7). This difference vanishes when the time step for each potential is constant.

Finally, by reverting to the x and v notation adopted at the beginning of the section AVI reads

$$v_a^{i+1/2} = v_a^i - \frac{1}{m_a} \sum_{k \in \mathscr{K}(i)} \frac{h_k^{i+1/2}}{2} \frac{\partial V_k}{\partial x_a}(x^i), \tag{8a}$$

$$x^{i+1} = x^i + (\theta^{i+1} - \theta^i)v^{i+1/2}, \tag{8b}$$

$$v_a^{i+1} = v_a^{i+1/2} - \frac{1}{m_a} \sum_{k \in \mathscr{K}(i+1)} \frac{h_k^{i-1/2}}{2} \frac{\partial V_k}{\partial x_a}(x^{i+1}), \tag{8c}$$

which reduces to VV when all time steps are identical.

It can also be verified that AVI is a generalization of the well-known r-RESPA [47]. To this end, it is enough to choose the time steps for each potential such that $h_{k+1}/h_k = r_k$ is an integer, for all $k \geqslant 1$. In that case, Eqs. (8a)–(8c) can be implemented as shown in Algorithm 2 in Appendix A. This algorithm is identical to r-RESPA.

2.1. Algorithm implementation

Since each of the potentials V_k has a different time step, a priority queue is used to determine the order in which the potentials are evaluated. The elements of this priority queue have the form (t_k^j, k), where t_k^j is the next time at which potential V_k needs to be evaluated, with the elements sorted in ascending order with respect to t_k^j. In case of equality of t_k^j for different ks, the ordering does not matter. As a result the element at the top gives the time of the next potential evaluation and the indices j and k corresponding to the time t_k^j. The AVI routine in Algorithm 1 below is a possible implementation, best tailored for problems with only a few different potentials with essentially all degrees of freedom as the arguments for each one of them. This is a typical situation encountered in the simulation of macromolecules with molecular dynamics. In contrast, a version of the algorithm better suited for finite-element-like simulations has already been introduced in [27]. In this latter case there are a large number of different potentials with only a few arguments each.

Algorithm 1. AVI algorithm

Input: θ^0; x^0; v^0; set of all potential times $t_{\{k\}}^{\{j\}}$
Output: $(\theta^{\{i\}}, x^{\{i\}}, v^{\{i\}})$, for all i
Initialization
$i = 0$

$v = v^0$; $x = x^0$; $\theta^{\text{old}} = \theta^0$
$F^{1/2} = F^{-1/2} = 0$
for all k **do**
    Push (t_k^0, k) into the priority queue Q
    $M_k = $ size of array $t_k^{\{j\}}$
end for
Integrate the system over the time interval $[0, T]$
while priority queue is not empty **do**
    Pop the top element (t_k^j, k) from Q
    $\theta^{\text{new}} = t_k^j$
    if $\theta^{\text{new}} > \theta^{\text{old}}$ **then**
        for all a **do** {Half-kick}
            $v_a = v_a + \frac{1}{2} \frac{F_a^{-1/2}}{m_a}$
        end for
        $x^i = x$; $v^i = v$; $\theta^i = \theta^{\text{old}}$
        $i = i + 1$
        for all a **do** {Half-kick}
            $v_a = v_a + \frac{1}{2} \frac{F_a^{1/2}}{m_a}$
        end for
        $x = x + (\theta^{\text{new}} - \theta^{\text{old}})v$ {Drift}
        $F^{1/2} = F^{-1/2} = 0$
    end if
    $\theta^{\text{old}} = \theta^{\text{new}}$
    if $j > 0$ **then**
        $F^{-1/2} = F^{-1/2} - (t_k^j - t_k^{j-1})\nabla V_k(x)$
    end if
    if $j < M_k$ **then**
        $F^{1/2} = F^{1/2} - (t_k^{j+1} - t_k^j)\nabla V_k(x)$
        Push (t_k^{j+1}, k) into the priority queue Q
    end if
end while
for all a **do** {Half-kick}
    $v_a = v_a + \frac{1}{2} \frac{F_a^{-1/2}}{m_a}$
end for
$x^i = x$; $v^i = v$; $\theta^i = \theta^{\text{old}}$

3. Stability of multi-step integrators

We begin by analyzing the stability of VV and r-RESPA. Similar analyses have been published elsewhere [39,1]. However, since we will show that the results for AVI extend this analysis, we briefly recall the main results regarding VV and r-RESPA (see e.g. [39,1] for a similar analysis).

Consider a system of n first-order ODEs:

$$\dot{x} = \mathbf{A}x, \quad x(0) = x_0.$$

Let $\mathbf{Q}$ be the propagation matrix representing the numerical integrator $x^{j+1} = \mathbf{Q}x^j$, where $\{x^0, x^1, \ldots, x^M\}$ is a time discretization of $x(t)$. Then the integrator represented by $\mathbf{Q}$ is stable if and only if its eigenvalues $\lambda_i(\mathbf{A})$ satisfy

$$|\lambda_i| \leqslant 1 \tag{9}$$

and are semi-simple[1] when equal.

We should note that a linear stability analysis does not necessarily capture all possible instabilities. Non-linearities can play an important role in rendering linearly stable schemes unstable, as shown in [42].

We now focus on the propagation matrix $\mathbf{Q}_{\text{VV}}$ for a 1-D harmonic oscillator

$$\ddot{x} + \Lambda x = 0, \quad x(0) = x_0, \quad \dot{x}(0) = v_0,$$

integrated with VV. The matrix $\mathbf{Q}_{\text{VV}}$ acts on phase-space variables x and $\dot{x}$. It is equal to:

---

[1] An eigenvalue is semi-simple if the number of independent eigenvectors corresponding to that eigenvalue is equal to its algebraic multiplicity.

$$\mathbf{Q}_{VV} = \begin{bmatrix} 1 - \frac{h^2}{2}\Lambda & h \\ -h\Lambda\left(1 - \frac{h^2}{4}\Lambda\right) & 1 - \frac{h^2}{2}\Lambda \end{bmatrix}.$$

It can be shown that the eigenvalues of $\mathbf{Q}_{VV}$ satisfy the stability condition if and only if

$$h < \frac{2}{\sqrt{\Lambda}}. \tag{10}$$

The range of stable time steps can also be found by looking at the shadow Hamiltonian for the numerical integrator. Obtained from backward error analysis, the shadow Hamiltonian for a symplectic integrator is such that the trajectory it generates matches exactly the numerical integrator at each time step. Shadow Hamiltonians are presented and discussed in greater detail in [17,25,34,18]. Here the shadow Hamiltonian will be constructed for $\mathbf{Q}_{VV}^2$ instead of $\mathbf{Q}_{VV}$. The reason is that $\mathbf{Q}_{VV}$ may have negative eigenvalues in which case the shadow Hamiltonian is complex-valued. However, by considering $\mathbf{Q}_{VV}^2$ the eigenvalues are always positive and the resulting shadow Hamiltonian is always real. The shadow Hamiltonian for the integrator with propagator matrix $\mathbf{Q}_{VV}^2$ is

$$\widetilde{H}_{VV}(q,p_q) = \begin{cases} \left(\frac{p_q^2}{2\gamma} + \frac{1}{2}\gamma\Lambda q^2\right)\frac{\cos^{-1}\left(1 - \frac{h^2}{2}\Lambda\right)}{h\sqrt{\Lambda}} & \text{if } h < 2/\sqrt{\Lambda} \\ -\frac{1}{2}p_q^2 & \text{if } h = 2/\sqrt{\Lambda}, \\ \left(-\frac{p_q^2}{2\gamma} + \frac{1}{2}\gamma\Lambda q^2\right)\frac{\cosh^{-1}\left(\frac{h^2}{2}\Lambda - 1\right)}{h\sqrt{\Lambda}} & \text{if } h > 2/\sqrt{\Lambda} \end{cases}$$

where p_q is the conjugate momentum of the spatial coordinate q and

$$\gamma = \sqrt{\left|1 - \left(\frac{h}{2}\sqrt{\Lambda}\right)^2\right|}.$$

When $h < 2/\sqrt{\Lambda}$ the shadow Hamiltonian agrees with the result from [34]. Noticing that the level sets of $\widetilde{H}_{VV}$ are ellipses if $h < 2/\sqrt{\Lambda}$ we conclude that VV is stable in this regime. However, if $h = 2/\sqrt{\Lambda}$ the level sets of $\widetilde{H}_{VV}$ are now lines whereas for $h > 2/\sqrt{\Lambda}$ the level sets are hyperbolas. In both cases these contours correspond to unstable trajectories. Therefore, VV is unstable if $h \geqslant 2/\sqrt{\Lambda}$.

To study the stability of multiple time step integrators, we start by examining the basic resonance mechanism for these integrators. Consider a 1-D harmonic oscillator with the splitting $\Lambda = \Lambda_1 + \Lambda_2$ where $\Lambda_1 \geqslant \Lambda_2 > 0$. Hereafter the spring with spring constant Λ_1 will be referred to as the stiff spring and Λ_2 as the soft spring. We consider then the case in which the stiff spring is integrated exactly. This results in a sinusoidal trajectory in time with constant energy as long as the soft spring is not accounted for. The time-integration scheme for the soft spring modifies this trajectory by imparting an impulse (or "kick") on the oscillator at time intervals of length h_2, which makes the momentum instantaneously jump to a new value. Between any two consecutive impulses, the trajectory is still sinusoidal in time with constant energy. If h_2 happens to be equal to an integer multiple of the half-period of the fast oscillator, then a resonance occurs, as clearly illustrated by the phase diagram in Fig. 3. In this case the initial conditions are $x = 1$ and $\dot{x} = 0$. The soft spring impulse is then always applied when $x = 1, \dot{x} \leqslant 0$ or $x = -1, \dot{x} \geqslant 0$. In both cases, the sign of the force is such that it results in a net growth in speed, bringing the oscillator to continue moving on a larger ellipse with increased energy. This leads to a resonant behavior. An analog behavior will be observed for values of h_2 that are close to but not exactly equal to half of the period of the stiff oscillator, as we shall see next.
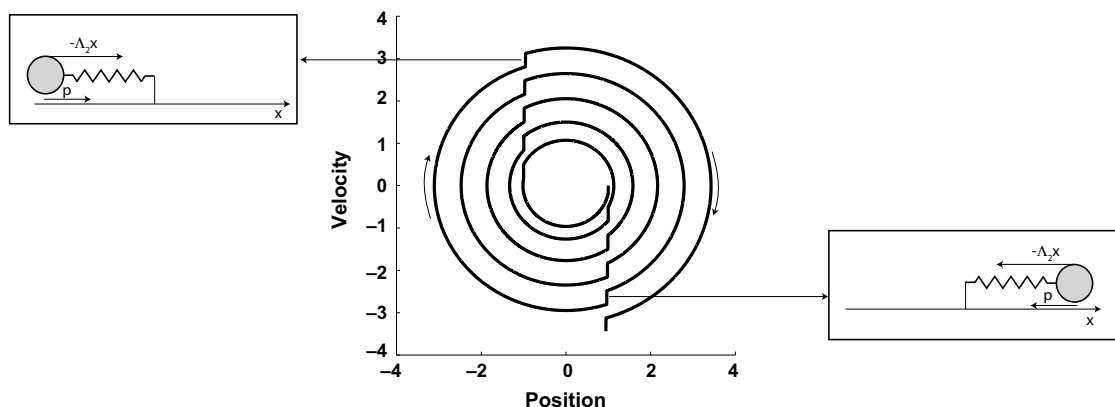
Fig. 3. Phase plane diagram of harmonic oscillator hit with a velocity impulse every half-period. The initial conditions are $x = 1$ and $\dot{x} = 0$. Notice that in this case the impulses result in a net energy growth, as evidenced by the radius of the circle representing the trajectory of the harmonic oscillator.

With this resonance mechanism in mind we now proceed to examine the effect of integrating the stiff spring with a discrete time step h_1. Consider the case in which $h_2 = ph_1$ where p is an integer. A single integration step of length h_2 can be decomposed as (see Eqs. (8)):

$$\begin{bmatrix} x^{j+1} \\ v^{j+1} \end{bmatrix} = \mathbf{V}_{\text{slow}}(\mathbf{Q}_{\text{fast}})^p \mathbf{V}_{\text{slow}} \begin{bmatrix} x^j \\ v^j \end{bmatrix} \stackrel{\text{def}}{=} \mathbf{Q}_{\text{r-RESPA}} \begin{bmatrix} x^j \\ v^j \end{bmatrix},$$

where

$$\mathbf{V}_{\text{slow}} = \begin{bmatrix} 1 & 0 \\ -\frac{h_2}{2}\Lambda_2 & 1 \end{bmatrix}$$

and

$$\mathbf{Q}_{\text{fast}} = \begin{bmatrix} 1 - \frac{h_1^2}{2}\Lambda_1 & h_1 \\ -h_1\Lambda_1\left(1 - \frac{h_1^2}{4}\Lambda_1\right) & 1 - \frac{h_1^2}{2}\Lambda_1 \end{bmatrix}.$$

Since $\mathbf{Q}_{\text{r-RESPA}}$ is the product of matrices each with determinant 1, its determinant is also 1. Therefore, when $|\operatorname{Tr}(\mathbf{Q}_{\text{r-RESPA}})| < 2$, the two eigenvalues are distinct complex conjugates lying on the unit circle. Hence the integrator is stable.

When $|\operatorname{Tr}(\mathbf{Q}_{\text{r-RESPA}})| = 2$, the two eigenvalues of $\mathbf{Q}_{\text{r-RESPA}}$ are identical, and equal to 1 or −1. Since stability requires the eigenvalue to be semi-simple in that case, it follows that the algorithm is stable if and only if $\mathbf{Q}_{\text{r-RESPA}} = \pm\mathbf{I}$, where $\mathbf{I}$ is the identity matrix. This leads to $h_1 = h_2 = 0$. Hence, the case $|\operatorname{Tr}(\mathbf{Q}_{\text{r-RESPA}})| = 2$ is always unstable.

Henceforth we shall assume that the stiff spring integrator is itself stable, i.e. that $h_1^2\Lambda_1 < 4$. The trace can then be expressed in terms of an invertible function $\theta : [0, 2/\sqrt{\Lambda_1}] \mapsto [0, \pi]$, $\theta(h_1)$, such that:

$$\cos\theta = 1 - \frac{h_1^2}{2}\Lambda_1, \quad \sin\theta = h_1\sqrt{\Lambda_1\left(1 - \frac{h_1^2}{4}\Lambda_1\right)}. \tag{11}$$

Denote:

$$\mathbf{G} = \begin{bmatrix} 1 & 0 \\ 0 & \sqrt{\Lambda_1\left(1 - \frac{h_1^2}{4}\Lambda_1\right)} \end{bmatrix}, \quad \text{and} \quad \mathbf{R}(\theta) = \begin{bmatrix} \cos\theta & \sin\theta \\ -\sin\theta & \cos\theta \end{bmatrix}.$$

Then it can be shown that $\mathbf{Q}_{\text{fast}} = \mathbf{G}\mathbf{R}(\theta)\mathbf{G}^{-1}$, and so

$$(\mathbf{Q}_{\text{fast}})^p = \mathbf{G}\mathbf{R}(p\theta)\mathbf{G}^{-1}, \tag{12}$$

since $\mathbf{R}(\theta)$ is the rotation matrix. In this formulation an effective angular frequency can be defined as $\omega_{\text{eff}}(h_1) = \theta/h_1$ so the effective period is given by $T_{\text{eff}} = 2\pi/\omega_{\text{eff}} = 2\pi h_1/\theta$. Using this alternative form for $\mathbf{Q}_{\text{fast}}$ we find that

$$\operatorname{Tr}(\mathbf{Q}_{\text{r-RESPA}}) = 2[\cos(p\theta) - \alpha\sin(p\theta)] \tag{13}$$

where

$$\alpha = \frac{h_2\Lambda_2}{2\sqrt{\Lambda_1\left(1 - \frac{h_1^2}{4}\Lambda_1\right)}}. \tag{14}$$

The stability condition $|\operatorname{Tr}(\mathbf{Q}_{\text{r-RESPA}})| < 2$ can also be gleaned from constructing the shadow Hamiltonian. As noted before for VV, to construct a real-valued shadow Hamiltonian we will consider the integrator with propagator matrix $\mathbf{Q}^2_{\text{r-RESPA}}$. The shadow Hamiltonian for this integrator is

$$\widetilde{H}_{\text{r-RESPA}}(q, p_q) = \begin{cases} \left(\frac{p_q^2}{2\gamma} + \frac{1}{2}\gamma\Lambda_1 q^2\right)\frac{\cos^{-1}\left(\frac{1}{2}\operatorname{Tr}(\mathbf{Q}_{\text{r-RESPA}})\right)}{h_2\sqrt{\Lambda_1}} & \text{if } |\operatorname{Tr}(\mathbf{Q}_{\text{r-RESPA}})| < 2 \\ s_{\text{Tr}}\left[\frac{\sin(p\theta)}{2p\sin\theta}\right]p_q^2 & \text{if } |\operatorname{Tr}(\mathbf{Q}_{\text{r-RESPA}})| = 2, \\ s_{\text{Tr}}\left(\frac{p_q^2}{2\gamma} - \frac{1}{2}\gamma\Lambda_1 q^2\right)\frac{\cosh^{-1}\left(\frac{1}{2}|\operatorname{Tr}(\mathbf{Q}_{\text{r-RESPA}})|\right)}{h_2\sqrt{\Lambda_1}} & \text{if } |\operatorname{Tr}(\mathbf{Q}_{\text{r-RESPA}})| > 2 \end{cases}$$

where p_q is the conjugate momentum of the spatial coordinate q and

$$s_{\text{Tr}} = \operatorname{sgn}(\operatorname{Tr}(\mathbf{Q}_{\text{r-RESPA}})),$$

$$\gamma = \frac{1}{\sin(p\theta)}\sqrt{1 - \left(\frac{h_1}{2}\sqrt{\Lambda_1}\right)^2}\sqrt{\left|1 - \left(\frac{1}{2}\operatorname{Tr}(\mathbf{Q}_{\text{r-RESPA}})\right)^2\right|}.$$

Since the level sets of $\widetilde{H}_{\text{r-RESPA}}$ are ellipses when $|\text{Tr}(\mathbf{Q}_{\text{r-RESPA}})| < 2$ we conclude that r-RESPA is stable in this regime. However, if $|\text{Tr}(\mathbf{Q}_{\text{r-RESPA}})| = 2$ the level sets of $\widetilde{H}_{\text{r-RESPA}}$ are now lines whereas for $|\text{Tr}(\mathbf{Q}_{\text{r-RESPA}})| > 2$ the level sets are hyperbolas. In both cases these contours correspond to unstable trajectories. Therefore, r-RESPA is unstable if $|\text{Tr}(\mathbf{Q}_{\text{r-RESPA}})| \geqslant 2$.

To determine what choice of time steps results in an unstable r-RESPA scheme, we start with the instability condition $|\text{Tr}(\mathbf{Q}_{\text{r-RESPA}})| \geqslant 2$. This condition is satisfied when

$$\left| \cos\left(\frac{2\pi h_2}{T_{\text{eff}}} + \phi \right) \right| \geqslant \frac{1}{\sqrt{1+\alpha^2}},$$

where

$$\cos(\phi) = \frac{1}{\sqrt{1+\alpha^2}}, \quad \sin(\phi) = \frac{\alpha}{\sqrt{1+\alpha^2}}.$$

A few observations about these conditions are now appropriate. If $h_2 = mT_{\text{eff}}/2$ for some integer m, the algorithm is unstable, in agreement with the example discussed before. In fact, the instability appears for a range of values of h_2 near $mT_{\text{eff}}/2$. Notably, these values always lie on only one side of $mT_{\text{eff}}/2$; they are always slightly smaller. Any value slightly larger than $mT_{\text{eff}}/2$ leads to stable schemes, albeit with energy oscillations of very large amplitude. Looking at Fig. 4a taking h_2 to be slightly smaller than $T_{\text{eff}}/2$ gives an unstable scheme as shown by the diverging trajectory. On the other hand Fig. 4b shows that taking h_2 to be slightly larger than $T_{\text{eff}}/2$ gives an ellipsoidal trajectory and hence the algorithm is stable. However, the high degree of stretching in the ellipse means that the energy exhibits large oscillations as a function of time.

Using the analysis developed thus far, the width and amplitude of these resonances can be determined. When $\alpha \ll 1$ and $h_1\sqrt{\Lambda_1} \ll 1$, the resonance width around $h_2 = mT_{\text{eff}}/2$, or interval length of resonant time steps h_2, is found to be proportional to the ratio $\Lambda_2/\Lambda_1^{3/2}$

$$l \approx \frac{T_{\text{eff}}}{\pi}\alpha = \frac{h_2 T_{\text{eff}}}{2\pi\sqrt{\Lambda_1\left(1 - \frac{h_1^2}{4}\Lambda_1\right)}}\Lambda_2 \approx m\pi\frac{\Lambda_2}{\Lambda_1^{3/2}}, \tag{15}$$
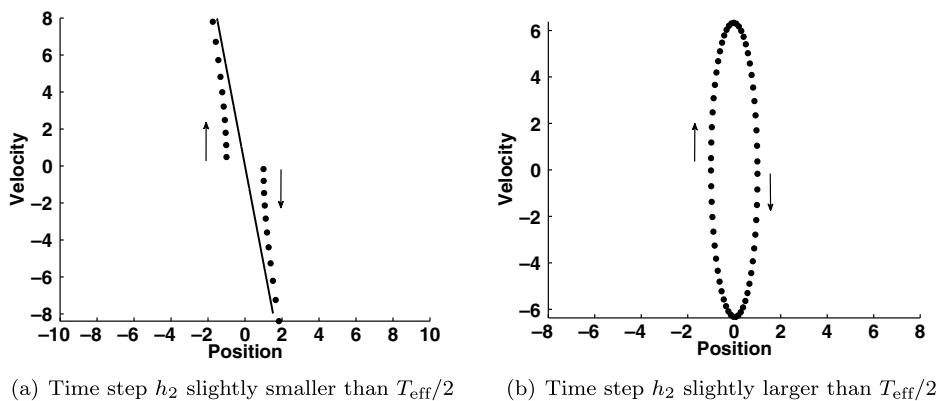
where the first approximation uses $\tan^{-1}(x) \approx m\pi + x$ for x small and the second assumes that for h_1 small $T_{\text{eff}} \approx 2\pi/\sqrt{\Lambda_1}$. Therefore, the resonance width decreases as the stiffness Λ_2 of the soft spring becomes softer relative to Λ_1. One implication of this is that resonances will persist even in the presence of a very soft spring but the probability of actually encountering them is low.

The resonance amplitude can be calculated by determining the magnitude of the largest eigenvalue. From the trace and determinant conditions the largest eigenvalue r_1 satisfies

$$|r_1| = \frac{1}{2}\left[|\text{Tr}(\mathbf{Q}_{\text{r-RESPA}})| + \sqrt{\text{Tr}(\mathbf{Q}_{\text{r-RESPA}})^2 - 4} \right].$$

The resonances occur for values of h_2 near integer multiples of $T_{\text{eff}}/2$

$$\frac{2\pi h_2}{T_{\text{eff}}} = m\pi - \beta,$$

(a) Time step h_2 slightly smaller than $T_{\text{eff}}/2$ (b) Time step h_2 slightly larger than $T_{\text{eff}}/2$

Fig. 4. Phase plane diagrams for two choices of the time step h_2 near $T_{\text{eff}}/2$ with the trajectories sampled every h_2 and denoted by the dots. The trajectory on the left alternates between the second and fourth quadrants. The arrows point in the direction of increasing time. Here $\Lambda_1 = 0.9$, $\Lambda_2 = 0.1$, and $T_{\text{eff}}/2 \approx 3.3115$. Left: Taking the time step h_2 to be slightly smaller than $T_{\text{eff}}/2$ ($h_2 = 3.30$) the energy of the system grows unbounded as shown by the trajectory diverging from the origin. Both branches of the trajectory are approaching the eigenvector of $\mathbf{Q}_{\text{r-RESPA}}$ corresponding to the larger unstable eigenvalue (solid line). Right: Taking the time step h_2 to be slightly larger than $T_{\text{eff}}/2$ ($h_2 = 3.32$) the resulting trajectory is a closed loop. As a result the scheme is stable however the stretched ellipse implies that the energy exhibits large oscillations.

where m is an integer and $0 < \beta < 2\alpha + O(\alpha^3)$. Assuming once again that α is small and that $h_1\sqrt{\Lambda_1} \ll 1$, we obtain the following approximation for $|r_1|$:

$$|r_1| \approx 1 + \beta\alpha - \frac{\beta^2}{2} + \sqrt{\frac{1}{3}\beta^4 - \beta^2 + \left(-\frac{4}{3}\beta^3 + 2\beta\right)\alpha + \beta^2\alpha^2}.$$

The maximum of $|r_1|$ is achieved near $\beta = \alpha$. With this, we get the following estimate for an upper bound on $|r_1|$:

$$\max_{\beta}|r_1| \approx 1 + \alpha + \frac{1}{2}\alpha^2 \approx 1 + \frac{m\pi}{2}\frac{\Lambda_2}{\Lambda_1}, \tag{16}$$

where we have only accounted for the linear term in α for the last expression. The amplitude of the resonance also decreases as the Λ_2 spring becomes softer relative to Λ_1. Note that the resonance amplitude is not maximum at $h_2 = mT_{\text{eff}}/2$, but near:

$$m\frac{T_{\text{eff}}}{2}\left(1 - \frac{1}{2}\frac{\Lambda_2}{\Lambda_1}\right).$$

4. Stability of AVI

We now turn our attention to the stability of the AVI algorithm. For two time steps h_1 and h_2 a propagation matrix $\mathbf{Q}_{\text{AVI}}$ can only be defined if there exists a synchronization point for the time integration of the two springs. This is the case when h_2/h_1 is a rational number p/q, where p and q are coprime integers. The two potentials then become synchronous at time $t = qh_2 = ph_1$. We will next prove a sufficient condition for the stability of the AVI algorithm, and numerically investigate the appearance of instabilities when the sufficient conditions are not satisfied.

Similarly to the study in Section 3, we need to calculate $\text{Tr}(\mathbf{Q}_{\text{AVI}})$. An exact equation for the trace can be found analytically for certain p and q (using a symbolic manipulation package for example). However, an equation valid for all p and q is obtained when a linearization in the variable Λ_2 is performed:

$$\text{Tr}(\mathbf{Q}_{\text{AVI}}) \approx 2[\cos(p\theta) - \alpha_q \sin(p\theta)], \tag{17}$$

where

$$\alpha_q = \frac{h_2\Lambda_2(q - \frac{q^2-1}{q}\frac{h_1^2}{6}\Lambda_1)}{2\sqrt{\Lambda_1(1 - \frac{h_1^2}{4}\Lambda_1)}}.$$

In fact, we provide an error bound for this approximation in the following proposition.

Proposition 1. *Assume that the fast integrator is stable, namely, $h_1^2\Lambda_1 < 4$. If time steps $h_1 < h_2$ satisfy that $h_2/h_1 = p/q$, for some p and q coprime integers, then the following inequality holds:*

$$\left|\text{Tr}(\mathbf{Q}_{\text{AVI}}) - 2[\cos(p\theta) - \alpha_q \sin(p\theta)]\right| < (2q\alpha_1)^2\left(1 + 2\alpha_1^2 + 2\alpha_1\sqrt{1 + \alpha_1^2}\right)^{\frac{q-2}{2}}, \tag{18}$$

where $\theta = h_1\omega_{\text{eff}}$ is defined in Eq. (11).

Before proving this result, let's consider some of its implications. Notice first that the analysis in Section 3 (see Eqs. (13) and (14)) corresponds to the case $q = 1$. In that case, the trace is exactly linear in Λ_2 and Eq. (17) is exact. Next, Eq. (18) provides a sufficient condition for stability, namely, the AVI algorithm is stable if

$$2|\cos(p\theta) - \alpha_q \sin(p\theta)| + (2q\alpha_1)^2\left(1 + 2\alpha_1^2 + 2\alpha_1\sqrt{1 + \alpha_1^2}\right)^{\frac{q-2}{2}} < 2. \tag{19}$$

To better illustrate when instabilities may be found, we write

$$\cos(p\theta) - \alpha_q \sin(p\theta) = \sqrt{1 + \alpha_q^2}\cos(p\theta + \phi)$$

with

$$\cos\phi = 1/\sqrt{1 + \alpha_q^2} \quad \text{and} \quad \sin\phi = \alpha_q/\sqrt{1 + \alpha_q^2}, \tag{20}$$

from where it follows that

$$\text{Tr}(\mathbf{Q}_{\text{AVI}}) \approx 2\sqrt{1 + \alpha_q^2}\cos(p\theta + \phi),$$

provided that the right-hand side in Eq. (18) is small enough. In these circumstances, a sufficient condition for the integrator to *be stable* is for $p\theta + \phi = qh_2w_{\text{eff}} + \phi$ to be sufficiently away from $m\pi$. This is more precisely stated in the following corollary:

Corollary 1. *Assume that the fast integrator is stable, namely, $h_1^2\Lambda_1 < 4$. Then, for any $\varepsilon > 0$ there exists $\eta > 0$ such that if $|p\theta + \phi - m\pi| > \varepsilon$ for all $m \in \mathbb{Z}$ and $qh_2\Lambda_2/\sqrt{\Lambda_1} < \eta$ then*

$$|\text{Tr}(\mathbf{Q}_{\text{AVI}})| < 2$$

and the AVI integrator is stable.

Proof 1. Observe first that the condition $|p\theta + \phi - m\pi| > \varepsilon$ for all $m \in \mathbb{Z}$ implies that $|\cos(p\theta + \phi)| < |\cos(\varepsilon)|$. Next, since $h_1^2\Lambda_1 < 4$, we have that $\alpha_1, \alpha_q \in \mathbb{R}$ and that $\alpha_q = O(q\alpha_1)$. Finally, notice that if $0 < qh_2\Lambda_2/\sqrt{\Lambda_1} < \eta$ then

$$0 < q\alpha_1 < \frac{\eta}{2\sqrt{1 - \frac{h_1^2}{4}\Lambda_1}} < \hat{\eta} \tag{21}$$

and the right-hand side of Eq. (18) satisfies

$$(2q\alpha_1)^2\left(1 + 2\alpha_1^2 + 2\alpha_1\sqrt{1 + \alpha_1^2}\right)^{\frac{q-2}{2}} < (2\hat{\eta})^2 \sup_{0 \leqslant \alpha_1 \leqslant \hat{\eta}} \left(1 + 2\alpha_1^2 + 2\alpha_1\sqrt{1 + \alpha_1^2}\right)^{\frac{\hat{\eta}}{2\alpha_1} - 1}$$
$$< (2\hat{\eta})^2 \exp(\hat{\eta}). \tag{22}$$

It is then always possible to choose $\eta > 0$ such that

$$|\text{Tr}(\mathbf{Q}_{\text{AVI}})| < 2|\cos(\varepsilon)|\sqrt{1 + \alpha_q^2} + (2q\alpha_1)^2\left(1 + 2\alpha_1^2 + 2\alpha_1\sqrt{1 + \alpha_1^2}\right)^{\frac{q-2}{2}}$$
$$< |2\cos(\varepsilon)|\sqrt{1 + \alpha_q^2} + (2\hat{\eta})^2 \exp(\hat{\eta})$$
$$< 2. \quad \square$$

This corollary generalizes the r-RESPA case ($q = 1$) for $qh_2\Lambda_2/\sqrt{\Lambda_1} \ll 1$, since in this case ϕ is also small and hence

the system is stable whenever $ph_1 = qh_2$ is away from $mT_{\text{eff}}/2$.

4.1. Proof of Proposition 1

We begin by constructing the propagation matrix $\mathbf{Q}_{\text{AVI}}$ over the time interval $t = 0$ to $t = qh_2 = ph_1$ as a composition of multiple elementary matrices. A simple expression of the resulting matrix product is in most cases difficult to obtain, so the key step in the proof is to perform a Taylor expansion for the trace of $\mathbf{Q}_{\text{AVI}}$ in terms of Λ_2, which leads to several simplifications. To this end,

$$\text{Tr}(\mathbf{Q}_{\text{AVI}})(\Lambda_2) = \text{Tr}(\mathbf{Q}_{\text{AVI}})(0) + \Lambda_2\frac{d\text{Tr}(\mathbf{Q}_{\text{AVI}})}{d\Lambda_2}\bigg|_{\Lambda_2=0} + \frac{\Lambda_2^2}{2}\frac{d^2\text{Tr}(\mathbf{Q}_{\text{AVI}})}{d\Lambda_2^2}\bigg|_{\Lambda_2^*}.$$

This is exact for some $0 < \Lambda_2^* < \Lambda_2$. We will show that:

$$\text{Tr}(\mathbf{Q}_{\text{AVI}})(0) + \Lambda_2\frac{d\text{Tr}(\mathbf{Q}_{\text{AVI}})}{d\Lambda_2}\bigg|_{\Lambda_2=0} = 2(\cos(p\theta) - \alpha_q\sin(p\theta)), \tag{23}$$

$$\left|\frac{\Lambda_2^2}{2}\frac{d^2\text{Tr}(\mathbf{Q}_{\text{AVI}})}{d\Lambda_2^2}\bigg|_{\Lambda_2^*}\right| < (2q\alpha_1)^2\left(1 + 2\alpha_1^2 + 2\alpha_1\sqrt{1 + \alpha_1^2}\right)^{\frac{q-2}{2}}. \tag{24}$$

These two equations prove our result.

We begin by defining a few matrices which are the building blocks of AVI:

$$\mathbf{V}_s = \begin{bmatrix} 1 & 0 \\ -\frac{h_2}{2}\Lambda_2 & 1 \end{bmatrix}, \quad \mathbf{V}_f = \begin{bmatrix} 1 & 0 \\ -\frac{h_1}{2}\Lambda_1 & 1 \end{bmatrix}, \quad \mathbf{U}_i = \begin{bmatrix} 1 & \frac{i}{q}h_1 \\ 0 & 1 \end{bmatrix},$$

$$\mathbf{Q}_f = \mathbf{V}_f\mathbf{U}_q\mathbf{V}_f = \begin{bmatrix} 1 - \frac{h_1^2}{2}\Lambda_1 & h_1 \\ -h_1\Lambda_1\left(1 - \frac{h_1^2}{4}\Lambda_1\right) & 1 - \frac{h_1^2}{2}\Lambda_1 \end{bmatrix},$$

$$\mathbf{Q}_s(m) = \mathbf{Q}_f^{-1}[\mathbf{V}_f\mathbf{U}_{q-m}\mathbf{V}_s\mathbf{V}_s\mathbf{U}_m\mathbf{V}_f].$$

Some of these definitions have been previously introduced. Matrices $\mathbf{V}_s$ and $\mathbf{V}_f$ correspond to kicks by the soft and the stiff springs, respectively, while matrix $\mathbf{U}_i$ represents a drift for a time interval of length ih_1/q. The matrix $\mathbf{Q}_f$ is the propagation matrix for a complete time step of the fast spring. Similarly, $\mathbf{Q}_f\mathbf{Q}_s(m)$ represents a kick-and-drift step with the stiff spring, followed by a kick by the soft spring, and a drift-and-kick step with the stiff spring. The drift time m/qh_1 ($\mathbf{U}_m$) is required to reach the time at which the soft spring kicks. After the soft kick, the system drifts for a time $(1 - m/q)h_1$ ($\mathbf{U}_{q-m}$) to reach the next time step for the stiff spring. The presence of $\mathbf{Q}_f^{-1}$ in the definition of $\mathbf{Q}_s$ was added for later convenience.

Let us introduce the sequence $m_i = ip \pmod{q}$, and

$$k_i = \left\lfloor \frac{ip}{q} \right\rfloor - \left\lfloor \frac{(i-1)p}{q} \right\rfloor, \quad 1 \leqslant i \leqslant q,$$

where $\lfloor x \rfloor$ stands for the largest integer smaller than x. The value of k_i is the number of time steps the stiff spring needs to perform between time steps $i - 1$ and i of the soft spring. Notice that this is exact because of the definition of $\mathbf{Q}_s$ with the factor $\mathbf{Q}_f^{-1}$. It then naturally follows that:

$$\sum_{i=1}^{q} k_i = p. \tag{25}$$

The propagation matrix $\mathbf{Q}_{AVI}$ is then given by:

$$\boxed{\mathbf{Q}_{AVI} = \mathbf{V}_s(\mathbf{Q}_f)^{k_q}\mathbf{Q}_s(m_{q-1})(\mathbf{Q}_f)^{k_{q-1}}\cdots\mathbf{Q}_s(m_1)(\mathbf{Q}_f)^{k_1}\mathbf{V}_s.}$$

This product leads to a complicated expression for arbitrary values of Λ_2, but it leads to a surprisingly simple one in the limit of very small Λ_2. Since $\mathbf{Q}_{AVI}$ is an infinitely smooth function of Λ_2, we can apply Taylor's theorem. The constant term is

$$\mathbf{Q}_{AVI}|_{\Lambda_2=0} = (\mathbf{Q}_f)^p.$$

The first derivative is equal to

$$\left.\frac{\partial\mathbf{Q}_{AVI}}{\partial\Lambda_2}\right|_{\Lambda_2=0} = \frac{\partial\mathbf{V}_s}{\partial\Lambda_2}(\mathbf{Q}_f)^p + (\mathbf{Q}_f)^p\frac{\partial\mathbf{V}_s}{\partial\Lambda_2} + \sum_{i=1}^{q-1}(\mathbf{Q}_f)^{p-\lfloor\frac{ip}{q}\rfloor}\frac{\partial\mathbf{Q}_s(m_i)}{\partial\Lambda_2}(\mathbf{Q}_f)^{\lfloor\frac{ip}{q}\rfloor},$$

where the derivatives are evaluated at $\Lambda_2 = 0$. We can calculate the linear part of the trace:

$$\mathrm{Tr}(\mathbf{Q}_{AVI}) = \mathrm{Tr}((\mathbf{Q}_f)^p) + \Lambda_2\mathrm{Tr}\left(2(\mathbf{Q}_f)^p\frac{\partial\mathbf{V}_s}{\partial\Lambda_2} + (\mathbf{Q}_f)^p\sum_{i=1}^{q-1}\frac{\partial\mathbf{Q}_s(m_i)}{\partial\Lambda_2}\right)\Bigg|_{\Lambda_2=0} + \mathrm{O}(\Lambda_2^2)$$

using the fact that $\mathrm{Tr}(\mathbf{AB}) = \mathrm{Tr}(\mathbf{BA})$. Since m_i is a permutation of $1, \ldots, q - 1$, we also have:

$$\mathrm{Tr}(\mathbf{Q}_{AVI}) = \mathrm{Tr}((\mathbf{Q}_f)^p) + \Lambda_2\mathrm{Tr}\left(2(\mathbf{Q}_f)^p\frac{\partial\mathbf{V}_s}{\partial\Lambda_2} + (\mathbf{Q}_f)^p\sum_{i=1}^{q-1}\frac{\partial\mathbf{Q}_s(i)}{\partial\Lambda_2}\right)\Bigg|_{\Lambda_2=0} + \mathrm{O}(\Lambda_2^2), \tag{26}$$

where i has been substituted instead of m_i in $\mathbf{Q}_s$. The term $\partial\mathbf{Q}_s(i)/\partial\Lambda_2$ at $\Lambda_2 = 0$ is a quadratic function of i which we write as

$$\left.\frac{\partial\mathbf{Q}_s(i)}{\partial\Lambda_2}\right|_{\Lambda_2=0} = \mathbf{A}_0 + \mathbf{A}_1 i + \mathbf{A}_2 i^2.$$

The coefficients can be obtained from the definition of $\mathbf{Q}_s(i)$:

$$\mathbf{A}_0 = -h_2\begin{bmatrix} 0 & 0 \\ 1 & 0 \end{bmatrix}, \quad \mathbf{A}_1 = \frac{h_1h_2}{q}\begin{bmatrix} 1 & 0 \\ h_1\Lambda_1 & -1 \end{bmatrix}, \quad \mathbf{A}_2 = \frac{h_1^2h_2}{q^2}\begin{bmatrix} -\frac{h_1\Lambda_1}{2} & 1 \\ -\frac{h_1^2\Lambda_1^2}{4} & \frac{h_1\Lambda_1}{2} \end{bmatrix}.$$

The sum can therefore be computed analytically:

$$\sum_{i=1}^{q-1}\left.\frac{\partial\mathbf{Q}_s(i)}{\partial\Lambda_2}\right|_{\Lambda_2=0} = (q-1)\mathbf{A}_0 + \frac{(q-1)q}{2}\mathbf{A}_1 + \frac{(q-1)q(2q-1)}{6}\mathbf{A}_2,$$

which, together with the value of $(\mathbf{Q}_f)^p$ in Eq. (12), enables the direct computation of the second term in Eq. (26):

$$\Lambda_2\mathrm{Tr}\left(2(\mathbf{Q}_f)^p\frac{\partial\mathbf{V}_s}{\partial\Lambda_2} + (\mathbf{Q}_f)^p\sum_{i=1}^{q-1}\frac{\partial\mathbf{Q}_s(i)}{\partial\Lambda_2}\right)\Bigg|_{\Lambda_2=0} = -\frac{h_2\Lambda_2\left(q - \left(\frac{q^2-1}{q}\right)\frac{h_1^2}{6}\Lambda_1\right)}{\sqrt{\Lambda_1(1 - \frac{h_1^2}{4}\Lambda_1)}}\sin(p\theta). \tag{27}$$

The first term in the same equation follows as

$$\mathrm{Tr}((\mathbf{Q}_f)^p) = \mathrm{Tr}(\mathbf{GR}(p\theta)\mathbf{G}^{-1}) = \mathrm{Tr}(\mathbf{R}(p\theta)) = 2\cos(p\theta).$$

Together with Eqs. (27) and (26), this proves Eq. (23).

We now establish a bound on the second derivative of $\mathrm{Tr}(\mathbf{Q}_{AVI})$. The first derivative at an arbitrary Λ_2 is given by:

$$\frac{\partial \mathbf{Q}_{AVI}}{\partial \Lambda_2} = \frac{\partial \mathbf{V}_s}{\partial \Lambda_2}(\mathbf{Q}_f)^{k_q}\mathbf{Q}_s(m_{q-1})(\mathbf{Q}_f)^{k_{q-1}}\cdots\mathbf{Q}_s(m_1)(\mathbf{Q}_f)^{k_1}\mathbf{V}_s$$
$$+ \mathbf{V}_s(\mathbf{Q}_f)^{k_q}\mathbf{Q}_s(m_{q-1})(\mathbf{Q}_f)^{k_{q-1}}\cdots\mathbf{Q}_s(m_1)(\mathbf{Q}_f)^{k_1}\frac{\partial \mathbf{V}_s}{\partial \Lambda_2}$$
$$+ \mathbf{V}_s\left[\sum_{i=1}^{q-1}(\mathbf{Q}_f)^{k_q}\mathbf{Q}_s(m_{q-1})(\mathbf{Q}_f)^{k_{q-1}}\cdots\frac{\partial \mathbf{Q}_s}{\partial \Lambda_2}(m_i)\cdots\mathbf{Q}_s(m_1)(\mathbf{Q}_f)^{k_1}\right]\mathbf{V}_s.$$

Using the facts that $\partial^2\mathbf{V}_s/\partial\Lambda_2^2 = 0$ and $\partial^2\mathbf{Q}_s(m)/\partial\Lambda_2^2 = 0$, we have

$$\frac{\partial^2 \mathbf{Q}_{AVI}}{\partial \Lambda_2^2} = 2\frac{\partial \mathbf{V}_s}{\partial \Lambda_2}(\mathbf{Q}_f)^{k_q}\mathbf{Q}_s(m_{q-1})(\mathbf{Q}_f)^{k_{q-1}}\cdots\mathbf{Q}_s(m_1)(\mathbf{Q}_f)^{k_1}\frac{\partial \mathbf{V}_s}{\partial \Lambda_2}$$
$$+ 2\frac{\partial \mathbf{V}_s}{\partial \Lambda_2}\left[\sum_{i=1}^{q-1}(\mathbf{Q}_f)^{k_q}\mathbf{Q}_s(m_{q-1})(\mathbf{Q}_f)^{k_{q-1}}\cdots\frac{\partial \mathbf{Q}_s}{\partial \Lambda_2}(m_i)\cdots\mathbf{Q}_s(m_1)(\mathbf{Q}_f)^{k_1}\right]\mathbf{V}_s$$
$$+ 2\mathbf{V}_s\left[\sum_{i=1}^{q-1}(\mathbf{Q}_f)^{k_q}\mathbf{Q}_s(m_{q-1})(\mathbf{Q}_f)^{k_{q-1}}\cdots\frac{\partial \mathbf{Q}_s}{\partial \Lambda_2}(m_i)\cdots\mathbf{Q}_s(m_1)(\mathbf{Q}_f)^{k_1}\right]\frac{\partial \mathbf{V}_s}{\partial \Lambda_2}$$
$$+ 2\mathbf{V}_s\left[\sum_{\substack{i,j=1\\i<j}}^{q-1}(\mathbf{Q}_f)^{k_q}\mathbf{Q}_s(m_{q-1})(\mathbf{Q}_f)^{k_{q-1}}\cdots\frac{\partial \mathbf{Q}_s}{\partial \Lambda_2}(m_j)\cdots\frac{\partial \mathbf{Q}_s}{\partial \Lambda_2}(m_i)\cdots\mathbf{Q}_s(m_1)(\mathbf{Q}_f)^{k_1}\right]\mathbf{V}_s. \tag{28}$$

In order to bound the second derivative, we need to recall some properties of matrix norms. Let $\mathbf{Q}$ be an $n \times n$ matrix, $n \in \mathbb{N}$, then

$$\|\mathbf{Q}\|_E^2 = \mathrm{Tr}(\mathbf{Q}^{\top}\mathbf{Q}) \quad \|\mathbf{Q}\|_2^2 = \sup_{\vec{x}\neq\vec{0}}\frac{\vec{x}^{\top}\mathbf{Q}^{\top}\mathbf{Q}\vec{x}}{\vec{x}^{\top}\vec{x}}$$

and it holds that $\|\mathbf{Q}\|_E = n^{1/2}\|\mathbf{Q}\|_2$. Additionally, for any two $n \times n$ matrices $\mathbf{P}$ and $\mathbf{Q}$, it holds that

$$\|\mathbf{PQ}\| \leqslant \|\mathbf{P}\|\|\mathbf{Q}\|$$

in any of the two norms. Finally, by Cauchy–Schwartz inequality we have

$$|\mathrm{Tr}(\mathbf{AB})| \leqslant \|\mathbf{A}\|_E\|\mathbf{B}\|_E \leqslant n\|\mathbf{A}\|_2\|\mathbf{B}\|_2. \tag{29}$$

We simplify the notations for clarity:

$$\mathbf{Q}_i = \mathbf{G}^{-1}\mathbf{Q}_s(m_i)\mathbf{G},$$
$$\mathbf{R}_i = \mathbf{R}(k_i\theta),$$

which transforms Eq. (28) into

$$\frac{\partial^2 \mathbf{Q}_{AVI}}{\partial \Lambda_2^2} = 2\frac{\partial \mathbf{V}_s}{\partial \Lambda_2}\mathbf{GR}_q\mathbf{Q}_{q-1}\mathbf{R}_{q-1}\cdots\mathbf{Q}_1\mathbf{R}_1\mathbf{G}^{-1}\frac{\partial \mathbf{V}_s}{\partial \Lambda_2}$$
$$+ 2\frac{\partial \mathbf{V}_s}{\partial \Lambda_2}\mathbf{G}\left[\sum_{i=1}^{q-1}\mathbf{R}_{k_q}\mathbf{Q}_{q-1}\mathbf{R}_{k_{q-1}}\cdots\frac{\partial \mathbf{Q}_i}{\partial \Lambda_2}\cdots\mathbf{Q}_1\mathbf{R}_{k_1}\right]\mathbf{G}^{-1}\mathbf{V}_s$$
$$+ 2\mathbf{V}_s\mathbf{G}\left[\sum_{i=1}^{q-1}\mathbf{R}_{k_q}\mathbf{Q}_{q-1}\mathbf{R}_{k_{q-1}}\cdots\frac{\partial \mathbf{Q}_i}{\partial \Lambda_2}\cdots\mathbf{Q}_1\mathbf{R}_{k_1}\right]\mathbf{G}^{-1}\frac{\partial \mathbf{V}_s}{\partial \Lambda_2}$$
$$+ 2\mathbf{V}_s\mathbf{G}\left[\sum_{\substack{i,j=1\\i<j}}^{q-1}\mathbf{R}_{k_q}\mathbf{Q}_{q-1}\mathbf{R}_{k_{q-1}}\cdots\frac{\partial \mathbf{Q}_j}{\partial \Lambda_2}\cdots\frac{\partial \mathbf{Q}_i}{\partial \Lambda_2}\cdots\mathbf{Q}_1\mathbf{R}_{k_1}\right]\mathbf{G}^{-1}\mathbf{V}_s.$$

We now simply denote $\|\cdot\|$ instead of $\|\cdot\|_2$. Noticing that $\|\mathbf{R}_i\| = 1$, we have that

$$\frac{1}{4}\left|\text{Tr}\left(\frac{\partial^2 \mathbf{Q}_{\text{AVI}}}{\partial \Lambda_2^2}\right)\right| \leqslant \left\|\mathbf{G}^{-1}\frac{\partial \mathbf{V}_s}{\partial \Lambda_2}\frac{\partial \mathbf{V}_s}{\partial \Lambda_2}\mathbf{G}\right\|\|\mathbf{Q}_1\|\cdots\|\mathbf{Q}_{q-1}\|$$

$$+ \left(\left\|\mathbf{G}^{-1}\mathbf{V}_s\frac{\partial \mathbf{V}_s}{\partial \Lambda_2}\mathbf{G}\right\| + \left\|\mathbf{G}^{-1}\frac{\partial \mathbf{V}_s}{\partial \Lambda_2}\mathbf{V}_s\mathbf{G}\right\|\right)\left[\sum_{i=1}^{q-1}\|\mathbf{Q}_1\|\cdots\|\mathbf{Q}_{i-1}\|\left\|\frac{\partial \mathbf{Q}_i}{\partial \Lambda_2}\right\|\|\mathbf{Q}_{i+1}\|\cdots\|\mathbf{Q}_{q-1}\|\right] \tag{30}$$

$$+ \|\mathbf{G}^{-1}\mathbf{V}_s\mathbf{V}_s\mathbf{G}\|\left[\sum_{\substack{i,j=1\\i<j}}^{q-1}\|\mathbf{Q}_1\|\cdots\|\mathbf{Q}_{i-1}\|\left\|\frac{\partial \mathbf{Q}_i}{\partial \Lambda_2}\right\|\|\mathbf{Q}_{i+1}\|\cdots\|\mathbf{Q}_{j-1}\|\left\|\frac{\partial \mathbf{Q}_j}{\partial \Lambda_2}\right\|\|\mathbf{Q}_{j+1}\|\cdots\|\mathbf{Q}_{q-1}\|\right].$$

This equation is obtained by a simple application of Eq. (29). It can then be verified by direct calculation that

$$\left\|\mathbf{G}^{-1}\frac{\partial \mathbf{V}_s}{\partial \Lambda_2}\frac{\partial \mathbf{V}_s}{\partial \Lambda_2}\mathbf{G}\right\| = 0, \tag{31}$$

$$\left\|\mathbf{G}^{-1}\mathbf{V}_s\frac{\partial \mathbf{V}_s}{\partial \Lambda_2}\mathbf{G}\right\| = \left\|\mathbf{G}^{-1}\frac{\partial \mathbf{V}_s}{\partial \Lambda_2}\mathbf{V}_s\mathbf{G}\right\| = \frac{\alpha_1}{\Lambda_2}, \tag{32}$$

$$\|\mathbf{G}^{-1}\mathbf{V}_s\mathbf{V}_s\mathbf{G}\| = \left(1 + 2\alpha_1^2 + 2\alpha_1\sqrt{1+\alpha_1^2}\right)^{\frac{1}{2}}, \tag{33}$$

$$\left\|\frac{\partial \mathbf{Q}_i}{\partial \Lambda_2}\right\| \leqslant \frac{2\alpha_1}{\Lambda_2}, \tag{34}$$

$$\|\mathbf{Q}_i\| \leqslant \left(1 + 2\alpha_1^2 + 2\alpha_1\sqrt{1+\alpha_1^2}\right)^{\frac{1}{2}}. \tag{35}$$

The last two inequalities use the fact that

$$|q^2 - i(q-i)h_1^2\Lambda_1| < q^2, \quad \text{for } 0 < h_1^2\Lambda_1 < 4 \quad \text{and} \quad 1 \leqslant i \leqslant q-1.$$

Applying these results in Eq. (30), we get

$$\frac{\Lambda_2^2}{2}\left|\text{Tr}\left(\frac{\partial^2 \mathbf{Q}_{\text{AVI}}}{\partial \Lambda_2^2}\right)\right|\Bigg|_{\Lambda_2^*} \leqslant 4q(q-1)\alpha_1^2\left(1 + 2\alpha_1^2 + 2\alpha_1\sqrt{1+\alpha_1^2}\right)^{\frac{q-2}{2}}$$

$$< (2q\alpha_1)^2\left(1 + 2\alpha_1^2 + 2\alpha_1\sqrt{1+\alpha_1^2}\right)^{\frac{q-2}{2}},$$

for any Λ_2^* such that $0 \leqslant \Lambda_2^* \leqslant \Lambda_2$, which proves Eq. (24). $\quad\square$

4.2. AVI and r-RESPA resonances

In the forthcoming sections we denote the effective half-period $T_{\text{eff}}(h_1)/2$ by $T_{1/2}(h_1)$. In Sections 4.2 and 4.3, all numerical results were obtained using extended precision arithmetic (53 digits were typically used), and we will define a *resonant interval* as an interval in the real line that contains all unstable time step values.

Given p and q, consider the problem of finding resonant points (h_1, h_2) along the line $h_2 = \frac{p}{q}h_1$. Our previous analysis predicts that the resonant points are approximately located at $h_2 = \frac{m}{q}T_{1/2}$ for $qh_2\Lambda_2/\sqrt{\Lambda_1} \ll 1$. The behavior for larger values of $qh_2\Lambda_2/\sqrt{\Lambda_1}$ was investigated numerically and presented next.
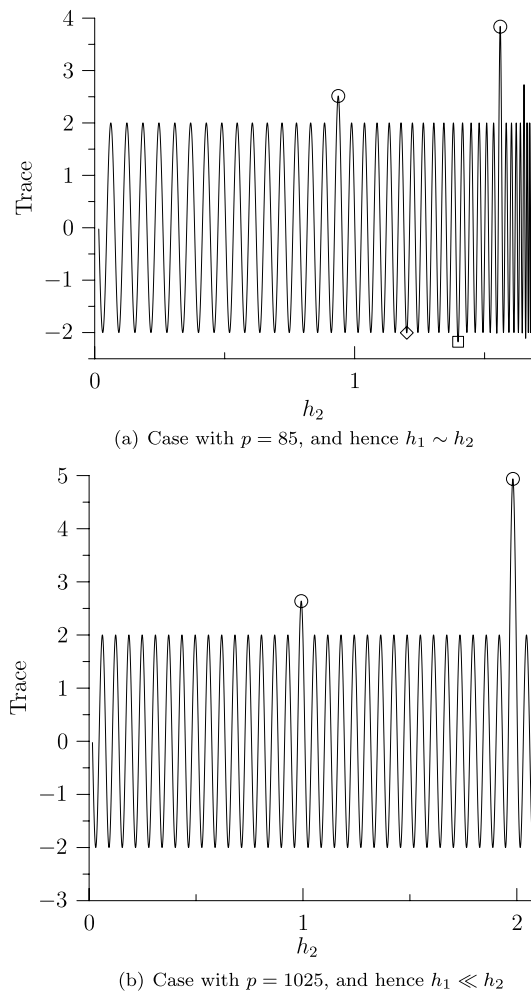
A typical result is illustrated in Fig. 5, which shows the value of $\text{Tr}(\mathbf{Q}_{\text{AVI}})$ as a function of h_2. We note that: (a) its value oscillates between -2 and 2 with a frequency close to $p\theta/h_2 \approx qw_{\text{eff}}$ and (b) an exhaustive examination of each local extremum reveals that the value of the trace at each one of them is a resonant point. This leads to resonances located at approximately $h_2 = mT_{1/2}(h_1)/q$, as before. Other numerical tests consistently displayed the same behavior as well. However, the presence of these two features in all examples does not follow from the result of Proposition 1. We conjecture that both characteristics are generally true, as expressed in the following statement, which remains to be proved:

Let $t_{p,q}(h_2)$ denote the value of $\text{Tr}(\mathbf{Q}_{\text{AVI}})$ evaluated at $(h_1, h_2) = (qh_2/p, h_2)$, for any $p > q$ coprime integers. Then, there exists a constant C independent of p and q such that for any $h_2 \in (0, 2p/(q\sqrt{\Lambda_1}))$ there exists an extremizer h_2^r of $t_{p,q}(h_2)$ that satisfies

$$h_2 \leqslant h_2^r < h_2 + \frac{C}{q\sqrt{\Lambda_1}}. \tag{36}$$

Additionally, all local extremizers are resonant points.

(a) Case with $p = 85$, and hence $h_1 \sim h_2$

(b) Case with $p = 1025$, and hence $h_1 \ll h_2$

Fig. 5. Trace of $\mathbf{Q}_{\text{AVI}}$ as a function of h_2, when $h_2 = ph_1/q$ for given values of p and q. Two different examples are shown, which differ in the value of p, but both adopt $q = 32$, $\Lambda_1 = \pi^2$, $\Lambda_2 = \pi^2/64$. When the value of the trace is outside of the interval $(-2, 2)$, the integrator is unstable. Zooming in on the regions where the trace is near 2 or -2 shows that, in each instance, there is an interval of instability. However, these instabilities are weak except when h_2 is near a multiple of $T_{1/2}$: these are depicted with circles. The main difference between the two cases is that the top plot shows additional large resonances besides the multiples of $T_{1/2}$. These are depicted by a square and a diamond.

Eq. (36) is motivated by the previous qualitative observation that the function $t_{p,q}(h_2)$ oscillates as h_2 changes with a frequency close to $qw_{\text{eff}}(qh_2/p)$. It then easily follows that the corresponding approximate period is bounded as

$$\frac{2\pi}{qw_{\text{eff}}(h_1)} = 2\pi \frac{h_1}{q\theta(h_1)} \leqslant \frac{2\pi}{q\sqrt{\Lambda_1}}. \tag{37}$$

The last inequality follows after noticing that

$$\theta(h_1) \geqslant \sqrt{\Lambda_1}h_1, \tag{38}$$

for $h_1 \in [0, \pi]$. The restriction $0 < h_2 < 2p/(q\sqrt{\Lambda_1})$ guarantees that only stable fast integrators are considered.

We explore next an important result that follow from assuming the previous conjecture to be true. This result states that the set of resonant points is dense in the set $H = \{(h_1, h_2) \in [0, 2/\sqrt{\Lambda_1}] \times \mathbb{R} \mid h_1 \leqslant h_2\}$. More precisely, this means that for any point $(h_1, h_2) \in H$ and $\varepsilon > 0$, it is possible to find a resonant point (h_1^r, h_2^r) such that $|h_1 - h_1^r| + |h_2 - h_2^r| < \varepsilon$.

To prove this result, consider $(h_1, h_2) \in H$ and $\varepsilon > 0$. Choose p and q such that $(h_1, ph_1/q) \in H$,

$$\left|\frac{p}{q}h_1 - h_2\right| < \frac{\varepsilon}{4} \quad \text{and} \quad \frac{C}{q\sqrt{\Lambda_1}} < \frac{\varepsilon}{4}. \tag{39}$$

It is evident that such a pair (p, q) exists, since p/q can be just adopted to be a rational approximation to h_2/h_1 with q large enough so as to satisfy the second condition in Eq. (39). Based on the above conjecture, we have that there exists a resonant point h_2^r such that

$$\left| h_2^r - \frac{p}{q} h_1 \right| < \frac{C}{q\sqrt{\Lambda_1}} < \frac{\varepsilon}{4}. \tag{40}$$

Together, Eqs. (39) and (40) imply that $|h_2 - h_2^r| < \varepsilon/2$. Since $h_1^r = h_2^r q/p$ and $q/p \leqslant 1$, we have from Eq. (40) that $|h_1 - h_1^r| < \varepsilon/2$, from where the result follows for any point in H' and hence in H.

We illustrate this result with an example next, in which we arbitrarily selected a set of time steps

$$(h_1, h_2) = (0.0090579193, 0.12698681)$$

and find a pair of resonant time steps nearby. In this case, we chose $p = 85158$ and $q = 6075$ such that $p/q \approx h_2/h_1$. An unstable point over the line $h_2 = ph_1/q$ was found at

$$(h_1^r, h_2^r) \approx (0.0090523798, 0.12690914).$$

At this point we have

$$\text{Tr}(\mathbf{Q}_{\text{AVI}}) \approx -2 - 1.2350353 \times 10^{-16},$$

which is a very weak resonance. By choosing an even larger value for q, and hence p, we could have found an even closer point.

A seemingly unusual consequence of the existence of a dense set of resonant points is that there are instabilities with arbitrarily small time steps (h_1, h_2). As an example, we chose $q = 10{,}000$, $p = 1024q + 1$, $\Lambda_1 = \pi^2$, $\Lambda_2 = \pi^2/64$. The first resonant point along the line $h_2 = ph_1/q$ was found at

$$h_1 \approx 9.6902126 \times 10^{-8}, \quad h_2 \approx 9.9227787 \times 10^{-5}.$$

At this resonant point, the trace is $-2 - 1.2873196 \times 10^{-32}$. The length of the instability interval is approximately 7×10^{-21}. Both features are depicted in Fig. 6, which shows the value of the trace of $\mathbf{Q}_{\text{AVI}}$ near its first minimizer. Notice that both h_1 and h_2 are much smaller than the upper bound for stability of the fast integrator, $2/\pi$. In general, the larger the values of p and q, the smaller the values of the first resonant set of time steps.

4.3. Unstable curves

We next discuss some additional aspects of the numerical experiments. As mentioned, resonances have been found at each local extremum, located at approximately $h_2 = mT_{1/2}(h_1)/q$. However, the vast majority of them are very weak. The largest resonances are near points for which $h_2/T_{1/2}$ is an integer. These resonances are the same type of resonances found in r-RESPA (see result in Section 3 for r-RESPA), and are indicated using a circle in Fig. 5.

In between the strong resonances near $h_2 = iT_{1/2}$ and $h_2 = (i + 1)T_{1/2}$ there are $q - 1$ weaker ones. We number the resonances consecutively along the line $h_2 = \frac{p}{q}h_1$ as h_2 grows with an index $m = 1, 2, \ldots$. With this convention, r-RESPA resonances correspond to $m = 0 \mod(q)$. The next largest resonances were observed to consistently correspond approximately to $m = \pm p \mod(q)$. More generally, let a, $\lfloor -q/2 \rfloor + 1 \leqslant a \leqslant \lfloor q/2 \rfloor$, be the unique integer such that $m = ap \mod(q)$ (with p and q having the greatest common denominator equal to 1). The strength of the resonance and the width of the associated resonant interval were consistently observed to *decrease* with $|a|$. In practice, this means that resonances with low values of $|a|$, such as $a = 0$, $a = 1$ and $a = -1$, are the ones which are most likely to be encountered, since the others are very narrow. In Fig. 5a the square corresponds to $a = 1$ and the diamond corresponds to $a = -1$.
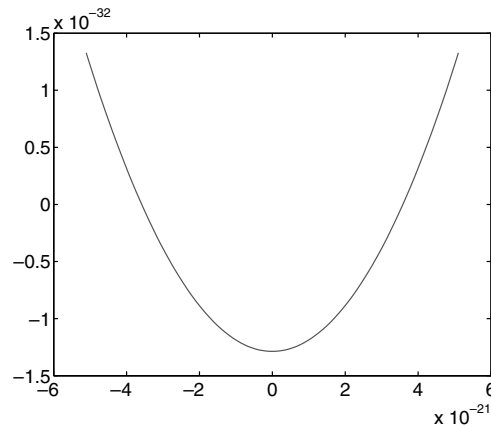
Fig. 6. Trace of $\mathbf{Q}_{\text{AVI}} + 2$ as a function of $h_2 - h_2^0$, with $h_1 = qh_2/p$ and $h_2^0 \approx 9.9227787 \times 10^{-5}$ being the smallest unstable value. The rest of the parameters for this calculation are: $q = 10{,}000$, $p = 1024q + 1$, $\Lambda_1 = \pi^2$, $\Lambda_2 = \pi^2/64$. Negative values on the vertical axis correspond to unstable values of h_2.

These observations are illustrated in more detail in Figs. 7 and 8, which show the width of the resonant interval and the amplitude for each resonance, respectively, as a function of the extremum index m. For this example we adopted $q = 1009$ and $p = 2439$. In general, the width of each resonance is highly correlated with the magnitude of the trace. The r-RESPA resonances are shown with circles, and are indeed the dominant ones. The resonances for $a = -3, -2, -1, 1, 2, 3$ are shown with squares and are larger and wider. The remaining resonances are narrower and smaller (with a few exceptions). In this case all extrema were found to be unstable as well, and indeed there are exactly 1008 resonances between the two r-RESPA peaks. However, as emphasized by the number of decades spanned by the logarithmic vertical axis in Fig. 8, most resonances are extremely weak. For most of them it would take millions of time steps or more to observe any visible drift in the energy.

The fact that only resonances with relatively low value of $|a|$ are likely to be encountered is nicely displayed by the following numerical calculation. In this case, pairs of time steps are selected such that they are both integer multiples of a given grid spacing h. For this study we adopted $h = 0.0005$, $\Lambda_1 = \pi^2$, $\Lambda_2 = \pi^2/25$, $h \leqslant h_1 \leqslant 2/\pi$, and $h_2 \leqslant 3.5$. If the propagation matrix $\mathbf{Q}_{AVI}$ for a given pair of time steps (h_1, h_2) has a spectral radius greater than 1, the pair is marked by a dark point and the algorithm is unstable for that choice of time steps. Fig. 9 shows the resulting plot over the domain $[h, 2/\pi] \times [h, 3.5]$.

Let us consider first the top plot in Fig. 9. The first noteworthy feature is that dark points do not appear everywhere, as would be expected from the fact that resonant pairs form a dense set. Instead, some curves stand out in the midst of a non-uniform cloud of dark points. This is only an artifact of choosing a finite step size, $h = 0.0005$. Large resonant intervals are the only ones likely to be visible on a plot with a finite resolution. As h goes to zero, the figure would be filled with more and more dark dots and the lines would effectively "disappear".

Approximate equations for these curves can be derived based on the previous empirical observations. Each of the thick nearly "horizontal" lines in Fig. 9 correspond to a different integer value of $h_2/T_{1/2}$, the r-RESPA resonances. The remaining curves are clearly narrower resonances, which we shall next see that correspond to low values of $|a|$.

Recall that a satisfies that $m = ap \mod(q)$, from where it follows that $m = ap + bq$ for some integer b. Consequently, if $ph_1 = qh_2$, the resonance condition $qh_2 \approx mT_{1/2}$ is satisfied if and only if

$$\frac{b}{h_2} \approx \frac{1}{T_{1/2}} - \frac{a}{h_1}. \tag{41}$$

For given values of a and b this is the equation of a curve in the (h_1, h_2)-plane.

In Fig. 9 (bottom row), we plotted the curves with $a = 0$ using thick solid lines (r-RESPA case), $a = 1$ with dotted lines, $a = 2$ with the dashed lines, and $a = -1$ with thin solid lines; b was varied to obtain several curves. The agreement with the location of the resonant points found numerically (Fig. 9, top row) is excellent. This comparison highlights the importance of $|a|$ in determining the width of the resonant interval. It would be interesting to obtain an analytical relation between the two that extends the asymptotic results in Section 4.

## 5. Why are AVI resonances ubiquitous in molecular dynamics but not in solid dynamics simulations?

Resonances are strong and common in molecular dynamics but seldom appear in solid dynamics simulations. We now use the insight gained in the last two sections with the stability analysis of the one-degree of freedom system to provide an explanation of the startling differences encountered on the performance of AVI in molecular dynamics and solid dynamics
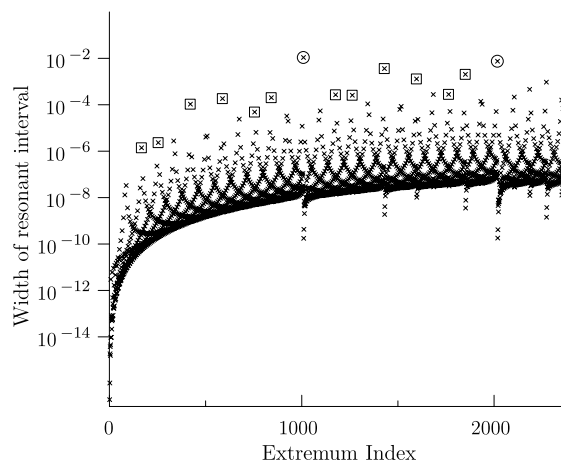
Fig. 7. Width of the resonant interval as a function of the resonance index for $q = 1009$, $p = 2439$, $\lambda_1 = \pi^2$ and $\lambda_2 = (\pi/8)^2$. The vertical axis is in logarithmic scale. Resonances of the r-RESPA type, in which h_2 is a multiple of $T_{1/2}$, are highlighted with circles. Resonances corresponding to $m = ap \mod(q)$, with $a = -3, -2, -1, 1, 2, 3$, are highlighted with squares. Extended precision arithmetic was adopted for this calculation to accurately compute the wide span of decades in the vertical axis, including the width of resonances 1 and 2 on the left.
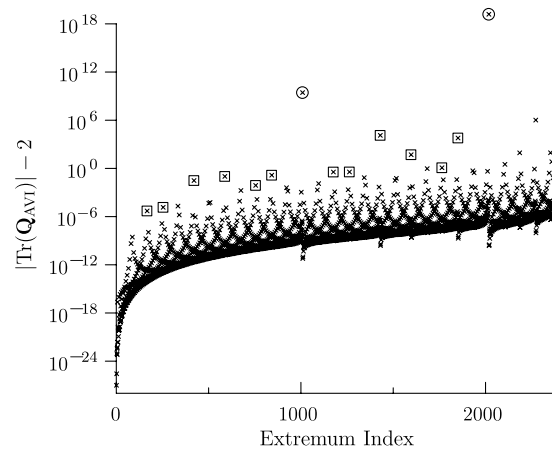
Fig. 8. Amplitude of each resonance, illustrated as $|\text{Tr}(\mathbf{Q}_{AVI})| - 2$ on the vertical axis, as a function of the resonance index for the case depicted in Fig. 7. The vertical axis is in logarithmic scale. As in Fig. 7, resonances of the r-RESPA type are highlighted with circles, while those corresponding to $m = ap \bmod(q)$, with $a = -3, -2, -1, 1, 2, 3$, are highlighted with squares.
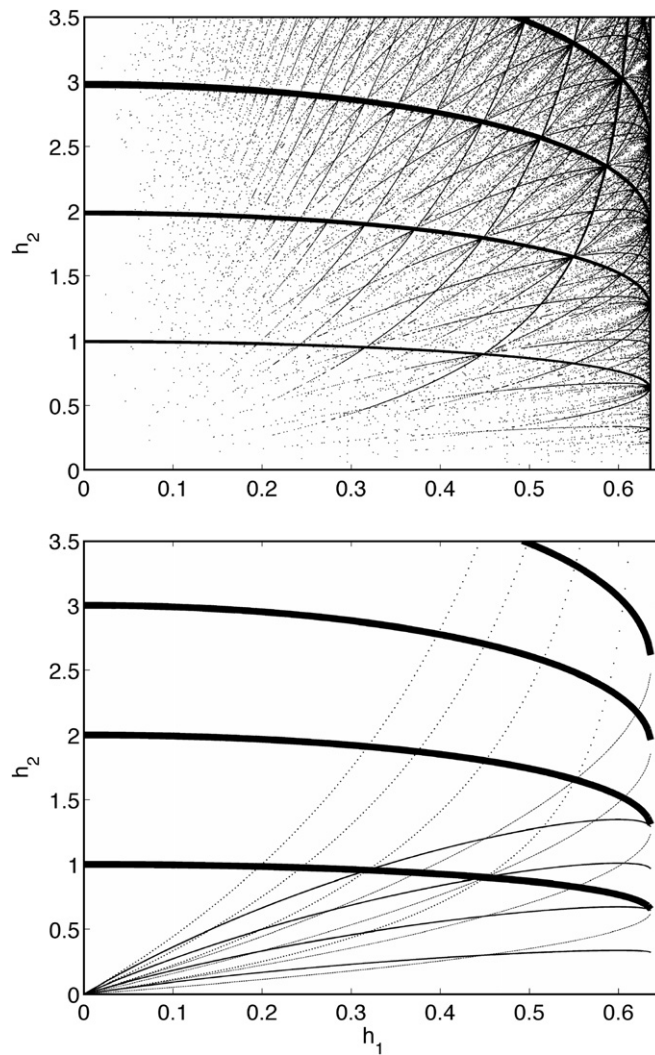
Fig. 9. AVI stability plot. Top figure: each unstable pair (h_1, h_2) is shown with a dot. Bottom figure: the theoretical prediction given by $b/h_2 = 1/T_{1/2} - a/h_1$ for some pairs of a and b is shown ($a = 0, -1, 1, 2$). The matching with the numerical results is excellent.

simulations. To this end, we performed numerical studies on two simplified systems. The first one resembles a molecular dynamics calculation; weak long-range forces are strongly coupled to local stiff springs. We analyzed the nature of the resonances by applying the results derived in the previous section. The second study considers the analog to a solid dynamics calculation performed with a finite-element discretization, and consists of a mesh of springs with different stiffnesses. Individual time steps for each spring are considered, with smaller time steps assigned to stiffer springs. We will see that in this case resonances are present but they are weak and very narrow, in stark contrast with the first example. This explains in part why such resonances are seldom seen in finite-element calculations.

5.1. Molecular dynamics analog

In molecular dynamics, particles are concurrently affected by potentials whose stiffnesses vary greatly. For example the bond potential is very stiff while the electrostatic potential at large distances is very soft. To study the resonant behavior in molecular dynamics we set up an analog using an infinite and periodic 2-D triangular *harmonic* lattice with a unit cell that consists of an $n \times n$ mesh of equal masses. To model the presence of short-range and long-range potentials, stiff springs are used to connect each pair of neighboring masses and a weak gravitational potential connects each mass to its nearest and second nearest neighbors; see Figs. 10a and b for the unit cell and a sketch of the interactions in the case $n = 4$.

The infinite lattice is formed by locating an identical mass with mass m at every position of the form $(iL, jL\sqrt{3}/2)$ with respect to a pair of Cartesian coordinate axes, for any $(i,j) \in \mathbb{Z}^2$, where L is the lattice parameter. The displacement of the mass at $(iL, jL\sqrt{3}/2)$ is denoted with $(u_{(i,j)}, v_{(i,j)})$, where u and v are the Cartesian components of the displacement vector. Periodic boundary conditions are imposed by restricting the set of possible displacements to those that are periodic with period nL, i.e. $u_{(i,j)} = u_{(i+n,j+n)}$, for all $(i,j) \in \mathbb{Z}^2$, and similarly for v.

Each mass is connected to its six neighboring masses with a spring. The potential energy for each one of these springs is

$$V_s(\ell) = \frac{k}{2}(\ell - L)^2, \tag{42}$$

where ℓ is the deformed length of the spring. The harmonic lattice corresponds to replacing each one of these springs by its quadratic approximation at $\ell = L$, the equilibrium length of the springs in the lattice in the absence of the gravitational potential. If $(\Delta u, \Delta v)$ indicates the Cartesian components of the difference in displacements between the two ends of the spring, the harmonic approximation to the potential is

$$V_s^h(\Delta u, \Delta v) = \frac{k}{2}(\Delta u \cos\theta + \Delta v \sin\theta)^2, \tag{43}$$

where θ is the angle the spring forms with the $(1, 0)$ direction in the undeformed lattice (see Appendix B for details). This is the potential used for each one of the springs in the numerical examples herein, for which we also adopted $n = 4$, $L = 1$, $m = 1$ and $k = 1$.

In the absence of the non-linear gravitational potential, the harmonic lattice possesses a constant symmetric stiffness matrix $\mathbf{K}$ independent of the displacements of the masses. It is then possible to find an orthonormal basis of eigenvectors for $\mathbf{K}$, the eigenmodes of the lattice. For the particular lattices considered here, there exist five groups of eigenmodes with natural frequencies $\omega = \sqrt{6}, \sqrt{5}, \sqrt{3}, \sqrt{2}$, and 1.

Finally, the gravitational potential used to represent the long-range interactions of the masses is given by

$$V_g(r) = -\frac{G}{\sqrt{r^2 + \epsilon}},$$

where r is the distance between the two masses, G is the gravitational constant, and ϵ is the softening term. To restrict $V_g(r)$ such that the potential affects only the nearest and second nearest neighbors of each mass $V_g(r)$ is premultiplied by a switching function $S(r)$. Define the modified potential as

(a) Short-range: stiff springs   (b) Long-range: gravitational potential
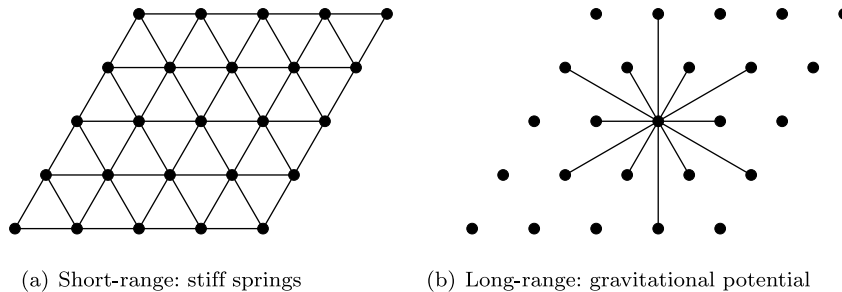
Fig. 10. Unit cell of a periodic harmonic lattice for the molecular dynamics analog. Each node in the graph represents a mass, and each edge an interaction between the two nodes at its ends. Short-range interactions are depicted on the left, while long-range ones are indicated on the right.

$$\widetilde{V}_g(r) = \begin{cases} S(r/r_c)V_g(r) & \text{if } r \leqslant r_c, \\ 0 & \text{if } r > r_c, \end{cases}$$

where

$$S(r) = 1 - 10r^3 + 15r^4 - 6r^5$$

and r_c is the cutoff radius. The function $S(r)$ is constructed such that $\widetilde{V}_g(0) = V_g(0)$ and $\widetilde{V}_g(r)$ is a C^2 smooth function. Nearest neighbors in the lattice are separated by the lattice parameter L, while second nearest neighbors by $\sqrt{3}L$, so by adopting $\sqrt{3}L < r_c \leqslant 2L$ each mass in the periodic harmonic lattice is only affected by the long-range potential through interactions with its nearest and second nearest neighbors. Fig. 11 compares these two versions of the gravitational potential. For our simulations we adopted $\widetilde{V}_g(r)$ as the weak long-range potential and set $G = 0.01$, $\epsilon = 1$, and $r_c = 1.85L$.
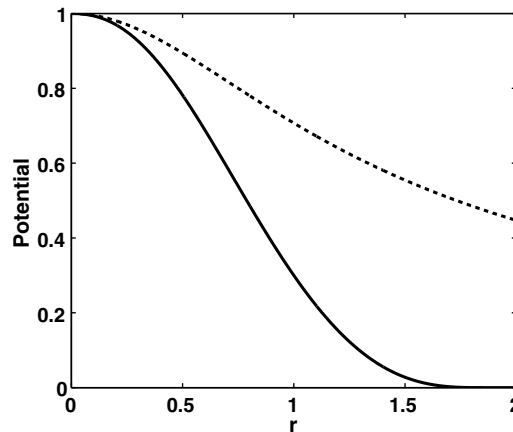
In the absence of the gravitational potential, each one of the eigenmodes of the lattice is itself an independent harmonic oscillator that does not interact with the remaining eigenmodes. The introduction of the long-range potential breaks this isolation, and induces a weak interaction among all eigenmodes. This is sketched in Fig. 12.

The total energy of each mass in the lattice is defined as the sum of its kinetic energy plus its potential energy contributions. The latter is formed by adding up one-half of the potential energy of each harmonic spring and each gravitational interaction attached to the mass. The total energy in the unit cell of the lattice is obtained as the sum of the total energy of each mass in the cell. For later use, it is also useful to specify a potential energy for each eigenmode in the unit cell, taken equal to $u_\omega^\mathsf{T} \mathbf{K} u_\omega / 2$, where u_ω is the displacement along the eigenmode with frequency ω.

For the numerical experiments we chose only two different time steps: a small time step h_1 for the springs, the stiff potentials; and a larger one h_2 for the gravitational potential, which is soft. In fact we chose $h_1 = 0.001$ so that the integration of each one of the eigenmodes of the harmonic lattice is nearly exact, because $h_1\omega \ll 1$ for any of the frequencies listed earlier. Since the gravitational potential is weak, its effect over each one of the eigenmodes is similar to that of the soft potential in the analysis in Sections 3 and 4, and hence we expect that if h_2 is close to an integer multiple of the half-period of any of the eigenmodes, a numerical resonance should be observed.

To search for resonances the time step h_2 for the gravitational potential was varied from 1 to 4 in increments of 0.005. Each integration was carried out until a maximum time of 500 was reached. At the end of each simulation the total energy of the unit cell lattice was recorded. The energy growth was computed as the difference between the total energy at the beginning and at the end of the simulation. These results are shown in Fig. 13, which also shows with solid dots the values of h_2 that correspond to integer multiples of the half-period for each one of the five different values of ω in the simulation. The close location of the spikes in the figure to the solid dots evidences that the expected numerical resonances are in fact occurring, triggered by the interaction of the gravitational potential with each one of the eigenmodes.

To further examine this resonant behavior, we chose the time step h_2 to be close to the half-period of the $\omega = \sqrt{6}$ and $\omega = \sqrt{5}$ eigenmodes. Their half-periods are $T_{1/2} = \pi/\sqrt{6} \approx 1.283$ and $T_{1/2} = \pi/\sqrt{5} \approx 1.405$, respectively. The total potential energy of the $\omega = \sqrt{6}$ eigenmodes for $h_2 = 1.285$ and the $\omega = \sqrt{5}$ eigenmodes for $h_2 = 1.41$ are shown in Figs. 14 and 15, along with the energy of the other eigenmodes. In both cases we observe an exponential-in-time growth of the total energy of the resonant eigenmodes, with a nearly unaffected evolution for the remaining ones. Only very late in the simulation does Fig. 15b display the beginning of an exponential-in-time growth of the energy of one of the remaining eigenmodes, as a result of the weak coupling between them and the already large amplitude of the $\omega = \sqrt{5}$ eigenmodes.

Fig. 11. Comparison of the two versions of the gravitational potential. The dotted line represents the gravitational potential $V_g(r) = -G/\sqrt{r^2 + \epsilon}$ with $G = 1$ and $\epsilon = 1$. The solid line is the modified potential $\widetilde{V}_g(r)$ which equals $-S(r/r_c)G/\sqrt{r^2 + \epsilon}$ for $0 \leqslant r \leqslant r_c$ (where $S(r) = 1 - 10r^3 + 15r^4 - 6r^5$) and zero for $r > r_c$. Here r_c is taken to be 1.85.
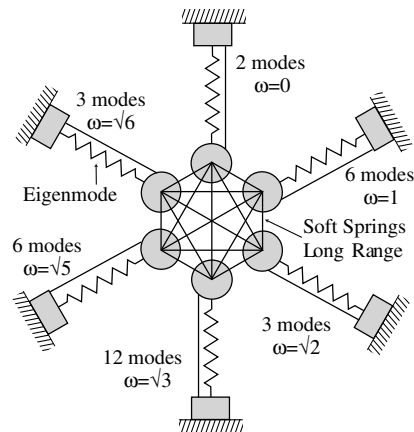
Fig. 12. Schematic interpretation of the lattice with a weak gravitational potential. In the absence of the gravitational potential each eigenmode in the lattice is an independent harmonic oscillator, depicted here as each one of the six wiggly springs. The gravitational potential breaks this isolation by connecting together the masses of each one of the eigenmodes via weak springs, depicted here with straight segments.
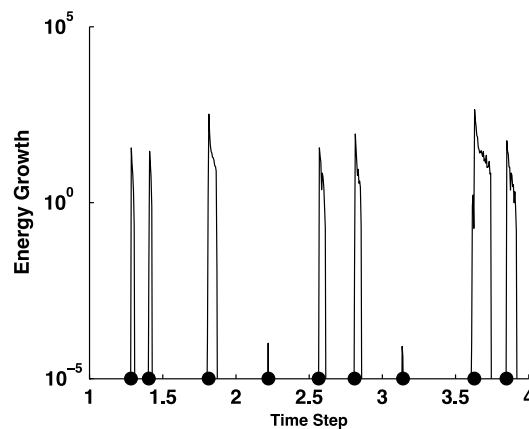
Fig. 13. Energy growth of the unit cell of the lattice due to numerical instabilities, as a function of the time step h_2 used to integrate the long-range gravitational potential. The energy growth at each time step value was computed as the difference between the energy at the beginning and at the end of each simulation. The solid dots represent the expected resonant time steps according to Section 3.

For a molecular dynamics simulation with a large number of atoms, integer multiples of the half-periods of the eigenmodes (also called the normal modes) are essentially closely packed over the real line. Therefore, in practice, it is virtually impossible to choose a value for h_2 that does not resonate with at least one of the eigenmodes, as illustrated with this example. Remarkably, the results on the very simple one-degree of freedom system in Sections 3 and 4 provide a clear explanation of the behavior observed in this example, and can be extrapolated to infer some aspects of the behavior for more complex systems. Fundamentally, what makes it possible is precisely the apparent lack of interaction among different modes of the lattice at the early stages of the resonant behavior.
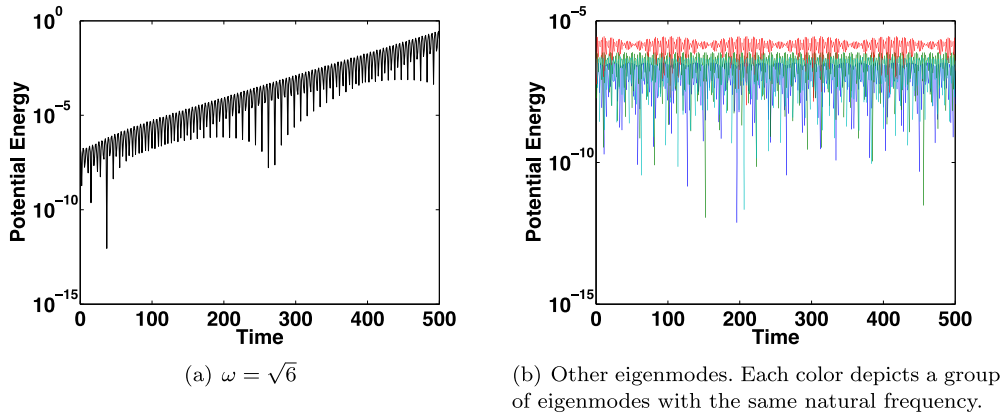
5.2. Solid dynamics analog

The second set of studies focus on a finite-element-like simulation, such as those used in solid mechanics for linear elastic problems. These cases usually lack a long-range force and are characterized by the existence of a range of element stiffness values, arising from the presence of different material properties and element sizes. Moreover, in many situations element stiffness values vary smoothly throughout the domain.

The potential energy for an elastic solid can be written as a sum of elemental contributions. An AVI discretization then naturally follows by assigning a possibly-different time step to each one of the elements (see [27]). The time step of each element is inversely proportional to its element stiffness value, and hence softer elements are allocated larger time steps.

If adaptive mesh refinement strategies are adopted, then the range of elemental stiffness values could possibly be very wide. In fact, some elements in the mesh are often integrated with time steps that are near an integer multiple of the half-period of a resonant mode of the structure. Why is then that the expected resonances are generally not encountered

(a) $\omega = \sqrt{6}$

(b) Other eigenmodes. Each color depicts a group of eigenmodes with the same natural frequency.

Fig. 14. Evolution of the potential energy for each group of eigenmodes for $h_2 = 1.285$, the time step of the weak long-range gravitational potential. It is seen that the eigenmodes whose half-period is $\pi/\sqrt{6} \approx 1.283$ are resonant with the long-range interaction, as expected from Section 3.

(a) $\omega = \sqrt{5}$

(b) Other eigenmodes. Each color depicts a group of eigenmodes with the same natural frequency.
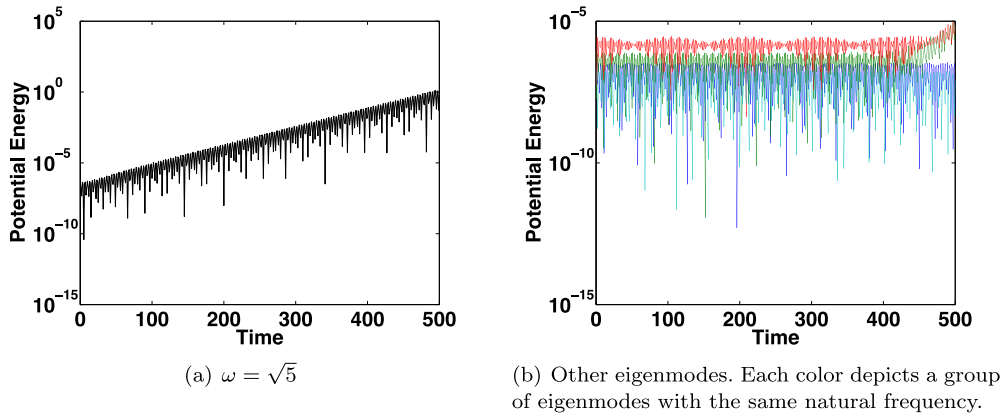
Fig. 15. Evolution of the potential energy for each group of eigenmodes for $h_2 = 1.41$, the time step of the weak long-range gravitational potential. It is seen that the eigenmodes whose half-period is $\pi/\sqrt{5} \approx 1.405$ are resonant with the long-range interaction, as expected from Section 3. Only by the end of the simulation does another group of eigenmodes display exponential-in-time growth of the potential energy, as a result of the weak coupling with the by-then-large amplitude oscillations of eigenmodes corresponding to $\omega = \sqrt{5}$ through the long-range potential.

in practice, as evidenced in the simulations in [26–28]? The answer is that the resonances are still present, as the foregoing analysis demonstrates. However, their amplitude and width are so small that they are hardly noticed in practice. The key difference with the molecular dynamics case in Section 5.1 lies in the absence of the long-range force. We shall illustrate these ideas with an example next.

We consider herein the same harmonic lattice adopted for the example in Section 5.1, in this case with no long-range gravitational potential and with a larger unit cell. The potential energy for each one of the springs connecting two neighboring masses is again determined by the harmonic approximation in Eq. (43), and displacements are restricted to be periodic, as specified earlier. When all springs are identical, the stiffness matrix of this lattice is identical to that obtained by identifying each triangle in the lattice as a piecewise linear finite-element made of an isotropic linear elastic material with Lame constants $\lambda = \mu = \sqrt{3}k/4$.

To represent the spatially varying stiffness values, we consider two different configurations of the springs: (1) only one spring in the unit cell is soft, while all the remaining ones are stiff (see Fig. 16a); and (2) a *core* of several soft springs, while the rest of the springs in the unit cell are stiff, as shown in Fig. 16b. In both instances, however, all springs but one are integrated with a small time step h_1, while one of the soft springs, the same in both cases, is integrated with a longer time step h_2 (see Fig. 16). For both types of lattices, the relevant eigenmodes to study the resonant behavior are those of the unit cell without the only soft spring integrated with a longer time step. We shall henceforth refer to these as the eigenmodes.

For all the forthcoming numerical examples we have adopted the values of $n = 7$, $L = 1$ and $k = 1$ for the stiff springs and $k = 0.33$ for the soft ones. We have purposely decided to avoid making the latter much smaller than the former, so as to highlight other types of phenomena that may also occur, as we shall next see. As in Section 5.1, we set $h_1 = 0.001$ so that it is much smaller than the period of any natural frequency in the lattice. The time step h_2 was varied from 1.3 to 1.6 in increments of 0.005. The total energy of the system was recorded at the end of a simulation with a total simulation time equal to 500.

(a) One soft spring   (b) Core of soft springs
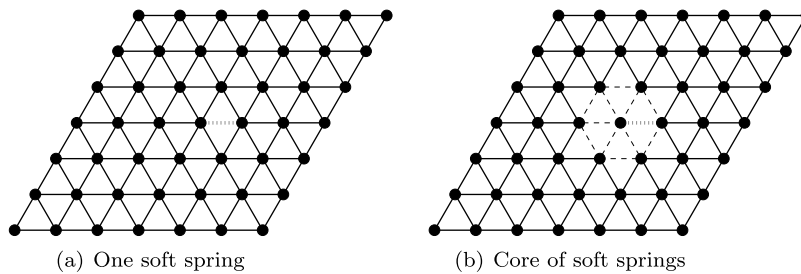
Fig. 16. Solid mechanics analogs using harmonic lattices. The soft spring integrated with a large time step h_2 is drawn with a dotted line. In the case depicted on the right the rest of the soft springs, which are integrated with a small time step h_1, are drawn with a dashed line. Stiff springs are drawn with a solid line.

Fig. 17 shows the total value of the energy at the end of each simulation as a function of h_2 for the first case, i.e. when only one soft spring is considered. The dots on the horizontal axis represent the half-period of the eigenmodes that fall within this time step range and are coupled to the soft spring (only three eigenmodes). As before, when the time step h_2 is near the half-period of one of the eigenmodes, resonant behavior was observed. However, in this case the resonance plot is not as simple as that in Section 5.1. In addition to the resonance instabilities that correspond to each one of the natural frequencies of the system, we observe a number of other peaks between the dots on the horizontal axis. This more complex profile results from a coupling between modes whose frequencies are close to one another given that the stiffness of the soft springs, 0.33, is not much smaller than that of the stiff ones, 1. These instabilities can be understood by analyzing a system of two harmonic oscillators joined by a third spring, in which the former are integrated with a smaller time step than the latter. We shall not expand on this observation, but just note that other types of resonances can be observed in addition to those arising from the excitation of a single eigenmode.

We now turn to the case where we have a core of soft springs, but in which only one of them is integrated with a long time step h_2. The total energy at the end of the simulation as a function of h_2 is shown in Fig. 18. The marks on the horizontal axis indicate the half-periods of those eigenmodes that fall within this time step range and have some non-negligible coupling with the soft spring integrated with a long time step. We observe that only the energy peak located near $h_2 = 1.56$ corresponds to one of the natural frequencies of the lattice (dot), with the other five peaks resulting from coupling between two or three eigenmodes. The marks at the energy peaks identify which modes are involved in the coupling that produces the observed instability. The eigenmode with half-period near 1.56 is involved in all five coupling events. For example the peak located at 1.45 is the product of coupling between the eigenmode with a half-period near 1.35 (triangle) and the eigenmode with a half-period near 1.56 (dot). In addition notice that the vertical energy scale is much shorter than that in Fig. 17. Resonances are still present, but they have been severely tamed and are much narrower than those in Fig. 17 when the soft core was absent.

To explain this result, it is convenient to take a look at the stiffness matrix of the entire lattice **K**. We can decompose **K** as $\mathbf{K} = \mathbf{K_1} + \mathbf{K_2}$ where $\mathbf{K_2}$ contains the one soft spring being integrated with the long time step and $\mathbf{K_1}$ contains all of the other springs (containing in fact both stiff and soft springs). The equation of motion is given by
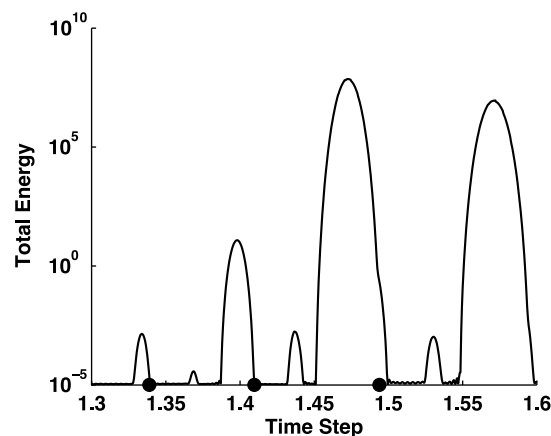
Fig. 17. Total energy of the harmonic lattice as a function of the time step adopted for the integration of the single soft spring in the lattice. The dots on the horizontal axis indicate integer multiples of half-periods of the eigenmodes in this time interval. Only those eigenmodes that are coupled to the soft spring are shown. Two types of resonances are observed, those that excite eigenmodes with the same natural frequency, recognized by the dots within them, and those that excite combinations of eigenmodes, as detailed in the text.
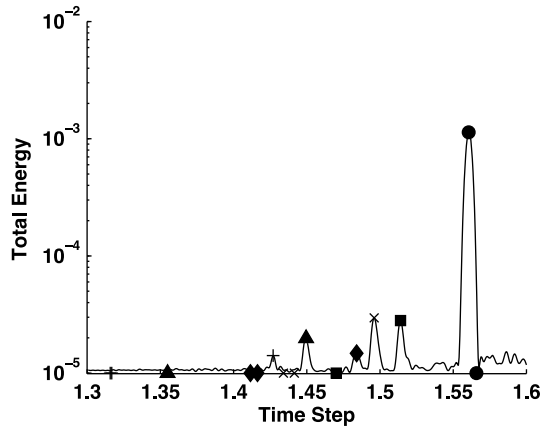
Fig. 18. Total energy of the harmonic lattice with a core of soft springs, in which only one of these springs is integrated with a longer time step. This time step is indicated on the horizontal axis. The marks on the horizontal axis indicate the half-periods of the eigenmodes that have a non-negligible coupling with the spring with the long-time step. Observe that only the energy peak denoted by the dot occurs at one of the natural frequencies of the lattice. The other peaks result from a coupling between modes with the same mark and the mode marked by a dot. For example the energy peak at 1.45 is due to a coupling between the mode with half-period 1.35 (triangle) and the mode with half-period 1.56 (dot). Notice that, in comparison with Fig. 17, the vertical axis has a drastically shorter energy scale, reflecting the fact that resonances in this case are much weaker and narrower than when only one soft spring is present in the entire lattice.

$$\ddot{x} + (\mathbf{K_1} + \mathbf{K_2})x = 0.$$

Now we can perform an eigenvector transformation for $\mathbf{K_1}$ which gives

$$\ddot{y} + (\mathbf{\Lambda} + \mathbf{V}^{\mathrm{T}}\mathbf{K_2}\mathbf{V})y = 0,$$

where $\mathbf{K_1} = \mathbf{V}\Lambda\mathbf{V}^{\mathrm{T}}$ and $y = \mathbf{V}^{\mathrm{T}}x$. This equation shows that, similar to the molecular dynamics case, there is a coupling between the soft spring with a long time step and the stiff modes. However, this coupling is given by matrix $\mathbf{V}^{\mathrm{T}}\mathbf{K_2}\mathbf{V}$. Because of the presence of the soft core, the entries in $\mathbf{V}^{\mathrm{T}}\mathbf{K_2}\mathbf{V}$ corresponding to stiff modes are very small, since as we shall see, stiff eigenmodes decay rapidly once they enter the region with soft springs. It then follows that the very small coupling terms in $\mathbf{V}^{\mathrm{T}}\mathbf{K_2}\mathbf{V}$ for the stiff modes effectively makes the soft spring integrated with time step h_2 even softer. As can be seen from Eqs. (15) and (16), the resulting resonances are still present, but they will be narrow and weak. Therefore, resonances are seldom observed in these types of simulations.

We showcase next the exponential decay of the high-frequency eigenvectors in the soft region through a one-dimensional example. Consider a system of 20 springs made of 10 springs with stiffness $k_1 = 8$ attached to 10 other springs with stiffness $k_2 = 1$, and identical masses between any two consecutive springs. The eigenvectors must satisfy the following equations:

$$k^{(i-1)}(x_i - x_{i-1}) - k^{(i)}(x_{i+1} - x_i) = \lambda x_i, \quad i = 2, \ldots, 20,$$

where x_i indicates the position of mass i and $k^{(i)}$ is the stiffness of spring i which connects masses i and $i+1$. A high-frequency eigenvector has $\lambda \gg k_2$. To estimate its decay in the region with soft springs, we assume that $|x_{i+1}| \ll |x_i|$ for $i \geqslant 12$. Then in this region

$$x_i \approx \frac{k_2}{2k_2 - \lambda}x_{i-1}.$$

This corresponds to a geometric decay with rate $\approx -k_2/\lambda$. Fig. 19 plots the first three stiffest eigenvectors. The circles correspond to the predicted geometric decay. We see that the prediction is quite accurate.
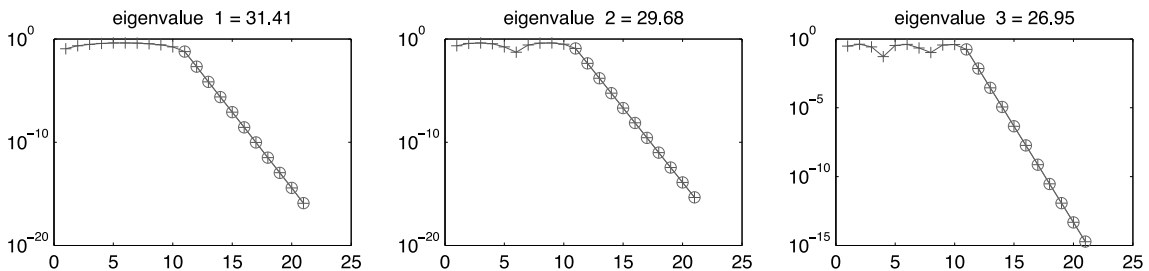
Fig. 19. Exponential decay of eigenvectors over core of soft springs. The circles are the analytical approximation of the decay. The agreement between the two is rather good.

This example demonstrates that stiff eigenvectors decay exponentially fast when they enter a soft region. A similar phenomenon should be valid in two-dimensional and three-dimensional meshes as well. In a mechanical problem then, soft regions of the mesh are only "locally" coupled to stiff ones. A soft element can still induce resonances in nearby stiff regions, but the strength of their coupling is exponentially small with the distance between them.

6. Summary

We studied the stability of AVI integrators and showed that results derived for the synchronous r-RESPA family of integrators can be generalized to asynchronous integrators such as AVI. We provided sufficient conditions for stability. We postulated that for a system of two 1-D springs with different stiffnesses an instability is observed when the synchronization time $ph_1 = qh_2$ is near a multiple of the half-period of the stiff potential. We motivated a conjecture that implies that the set of resonant time steps is dense, which was verified using systematic numerical tests. It also follows from the conjecture that arbitrarily small unstable time steps exist and, indeed, very small unstable time steps were found numerically. Most of these resonances were found to be very weak, and of little importance in practice. We characterized the strongest resonances through a family of curves parametrized by two integers, which reproduced the numerical results very well.

In addition, we examined the resonance behavior of AVI in molecular dynamics and solid mechanics. The main result is that resonances are easily observed in molecular dynamics due to the strong coupling between stiff modes and soft long-range forces (e.g. electrostatic forces). On the other hand, resonant behavior is rarely seen in solid mechanics because the smooth gradient of element stiffnesses leads to a very weak coupling and hence very narrow bands of resonant time steps.

Finally, the analyses herein are only concerned with the linear stability of the method. Other important resonances may be induced by the non-linearities in the system. Some results in this direction in the vicinity of stable equilibrium points are presented in [44]. Additionally, we note that classical techniques such as MOLLY [23], the two-force method [16,17], the isokinetic Nosé-Hoover chain RESPA [35], and Langevin equations [1,2,39] to enhance the stability of multiple time stepping schemes may be applicable to AVI, and may lead to improved robustness for the method. The two-force method is very promising since it removes all instabilities in the integrator. However, it currently has two drawbacks: it can be computationally expensive and it does not extend to three or more time steps without exponentially increasing its computational cost.

Appendix A. AVI algorithm in the r-RESPA case

The AVI algorithm in the r-RESPA case for three potentials is shown in Algorithm 2. This algorithm is identical to r-RESPA.

Algorithm 2. AVI Algorithm in the r-RESPA case for the case of three potentials

Input: x^0, v^0, h_1, r_1, r_2, n_{steps}
Output: (x^i, v^i), for all i
$i = 0$
$h_2 = r_1 h_1$
$h_3 = r_2 h_2$
$F = -h_1 \nabla V_1(x^0) - h_2 \nabla V_2(x^0) - h_3 \nabla V_3(x^0)$
for $n = 1$ to n_{steps} **do** {Outer most loop}
  for $j = 1$ to r_2 **do** {Loop for potential V_2}
    for $k = 1$ to r_1 **do** {Loop for potential V_1}
      for all a **do** {Half-kick}
        $v_a^{i+1} = v_a^i + \frac{1}{2} \frac{F_a}{m_a}$
      end for
      $x^{i+1} = x^i + h_1 v^{i+1}$ {Drift}
      $F = -h_1 \nabla V_1(x^{i+1})$
      if $k == r_1$ **then**
        $F = F - h_2 \nabla V_2(x^{i+1})$
      end if
      if $j == r_2$ **then**
        $F = F - h_3 \nabla V_3(x^{i+1})$
      end if
      for all a {Half-kick}
        $v_a^{i+1} = v_a^{i+1} + \frac{1}{2} \frac{F_a}{m_a}$
      end for
      $i = i + 1$
    end for
  end for
end for

Appendix B. Harmonic approximation of the lattice potential

The exact non-linear interaction potential between two masses connected by a spring is assumed to be given by:

$$V_s(r_1, r_2) = \frac{k}{2} \left(\sqrt{(x_2 - x_1)^2 + (y_2 - y_1)^2} - L \right)^2,$$

where k is the spring constant, $r_1 = (x_1, y_1)$ is the position of the first mass, $r_2 = (x_2, y_2)$ is the position of the second, and L is the equilibrium length of the spring. To derive a harmonic approximation, we first assume small displacements of the masses in the x and y directions. Then the position r_i of each node can be decomposed into an equilibrium position e_i and a displacement $d_i = (u_i, v_i)$. Consequently we define the x-displacement of the spring as $\Delta u = u_2 - u_1$ and the y-displacement as $\Delta v = v_2 - v_1$. V_s can now be rewritten as a function of Δu and Δv:

$$V_s(\Delta u, \Delta v) = \frac{k}{2} \left(\sqrt{(\Delta u + L_x)^2 + (\Delta v + L_y)^2} - L \right)^2$$

with $L_x = L \cos \theta$ and $L_y = L \sin \theta$ denoting the equilibrium lengths of the spring in the x and y directions, respectively, and θ representing the angle the spring forms with the $(1,0)$ direction. To approximate V_s, we find the Taylor expansion of V_s about $(\Delta u, \Delta v) = (0, 0)$. The resulting harmonic potential is

$$V_s^h(\Delta u, \Delta v) = \frac{k}{2} (\Delta u \cos \theta + \Delta v \sin \theta)^2.$$

Now we are ready to compute the stiffness matrix **K** for the 2-D triangular harmonic lattice using the harmonic potential V_s^h. We start by looking at one row of this matrix. For a given mass m_0 in the lattice, it interacts with six neighboring masses $m_1, \ldots, m_6$. These masses will be labeled in a counter-clockwise manner beginning with 1 for the mass located in the $(1,0)$ direction. As a result $\theta_i = (i - 1)\pi/6$ for $i = 1, \ldots, 6$. Then the six harmonic potentials are

$$V_1 = \frac{k}{2}(u_1 - u_0)^2, \quad V_4 = \frac{k}{2}(u_4 - u_0)^2,$$

$$V_2 = \frac{k}{2} \left[\frac{1}{2}(u_2 - u_0) + \frac{\sqrt{3}}{2}(v_2 - v_0) \right]^2, \quad V_5 = \frac{k}{2} \left[-\frac{1}{2}(u_5 - u_0) - \frac{\sqrt{3}}{2}(v_5 - v_0) \right]^2,$$

$$V_3 = \frac{k}{2} \left[-\frac{1}{2}(u_3 - u_0) + \frac{\sqrt{3}}{2}(v_3 - v_0) \right]^2, \quad V_6 = \frac{k}{2} \left[\frac{1}{2}(u_6 - u_0) - \frac{\sqrt{3}}{2}(v_6 - v_0) \right]^2$$

and the corresponding forces on mass m_0 due to potential V_i in the x and y directions are

$$F_{1x} = k(u_1 - u_0), \quad F_{1y} = 0,$$

$$F_{2x} = k \left[\frac{1}{4}(u_2 - u_0) + \frac{\sqrt{3}}{4}(v_2 - v_0) \right], \quad F_{2y} = k \left[\frac{\sqrt{3}}{4}(u_2 - u_0) + \frac{3}{4}(v_2 - v_0) \right],$$

$$F_{3x} = k \left[\frac{1}{4}(u_3 - u_0) - \frac{\sqrt{3}}{4}(v_3 - v_0) \right], \quad F_{3y} = k \left[-\frac{\sqrt{3}}{4}(u_3 - u_0) + \frac{3}{4}(v_3 - v_0) \right],$$

$$F_{4x} = k(u_4 - u_0), \quad F_{4y} = 0,$$

$$F_{5x} = k \left[\frac{1}{4}(u_5 - u_0) + \frac{\sqrt{3}}{4}(v_5 - v_0) \right], \quad F_{5y} = k \left[\frac{\sqrt{3}}{4}(u_5 - u_0) + \frac{3}{4}(v_5 - v_0) \right],$$

$$F_{6x} = k \left[\frac{1}{4}(u_6 - u_0) - \frac{\sqrt{3}}{4}(v_6 - v_0) \right], \quad F_{6y} = k \left[-\frac{\sqrt{3}}{4}(u_6 - u_0) + \frac{3}{4}(v_6 - v_0) \right].$$

Using these equations, **K** can be formed row-by-row.

References

[1] E. Barth, T. Schlick, Extrapolation versus impulse in multiple-timestepping schemes. II. Linear analysis and applications to Newtonian and Langevin dynamics, J. Chem. Phys. 109 (5) (1998) 1633–1642.
[2] E. Barth, T. Schlick, Overcoming stability limitations in biomolecular dynamics. I. combining force splitting via extrapolation with Langevin dynamics in LN, J. Chem. Phys. 109 (5) (1998) 1617–1632.
[3] T. Belytschko, Y. Lu, Convergence and stability analyses of multi-time step algorithm for parabolic systems, Comput. Methods Appl. Mech. Eng. 102 (1993) 179–198.
[4] T. Belytschko, R. Mullen, Mesh partitions of explicit–implicit time integrators, in: K.-J. Bathe, J. Oden, W. Wunderlich (Eds.), Formulations and Computational Algorithms in Finite Element Analysis, MIT Press, 1976, pp. 673–690.
[5] G. Benettin, A. Giorgilli, On the Hamiltonian interpolation of near-to-the-identity symplectic mappings with application to symplectic integration algorithms, J. Stat. Phys. 75 (5-6) (1994) 1117–1143.
[6] J. Biesiadecki, R. Skeel, Dangers of multiple time steps methods, J. Comput. Phys. 109 (1993) 318–328.

[7] W.J.T. Daniel, Analysis and implementation of a new constant acceleration subcycling algorithm, Int. J. Numer. Methods Eng. 40 (1997) 2841–2855.
[8] W.J.T. Daniel, The subcycled Newmark algorithm, Comput. Mech. 20 (1997) 272–281.
[9] W.J.T. Daniel, A study of the stability of subcycling algorithms in structural dynamics, Comput. Methods Appl. Mech. Eng. 156 (1) (1998) 1–13.
[10] W.J.T. Daniel, A partial velocity approach to subcycling structural dynamics, Comput. Methods Appl. Mech. Eng. 192 (3/4) (2003) 375–394.
[11] Y. Feng, K. Han, D. Owen, Asynchronous/multiple time integrators for impact and discrete systems, in: Proceedings of the Eighth International Conference on Computational Plasticity (COMPLAS VIII), Barcelona, Spain, 2005, pp. 5–8.
[12] A. Gravouil, A. Combescure, Multi-time-step explicit–implicit method for non-linear structural dynamics, Int. J. Numer. Methods Eng. 50 (1) (2001) 199–225.
[13] A. Gravouil, A. Combescure, Multi-time-step and two-scale domain decomposition method for non-linear structural dynamics, Int. J. Numer. Methods Eng. 58 (10) (2003) 1545–1569.
[14] H. Grubmüller, H. Heller, A. Windemuth, K. Schulten, Generalized Verlet algorithm for efficient molecular dynamics simulations with long-range interactions, Mol. Sim. 6 (1991) 121–142.
[15] E. Hairer, C. Lubich, The life-span of backward error analysis for numerical integrators, Numer. Math. 76 (1997) 441–462.
[16] E. Hairer, C. Lubich, Long-time energy conservation of numerical methods for oscillatory differential equations, SIAM J. Num. Anal. 38 (2) (2001) 414–441.
[17] E. Hairer, C. Lubich, G. Wanner, Geometric Numerical Integration: Structure-Preserving Algorithms for Ordinary Differential Equations, Springer, Verlag, 2002.
[18] G. Han, Y. Deng, J. Glimm, G. Martyna, Error and timing analysis of multiple time-step integration methods for molecular dynamics, Comp. Phys. Commun. 176 (2007) 271–291.
[19] M. Hochbruck, C. Lubich, A Gautschi-type method for oscillatory second-order differential equations, Numer. Math. 83 (3) (1999) 403–426.
[20] T. Hughes, W. Liu, Implicit-explicit finite elements in transient analysis: Stability theory, J. Appl. Mech. 78 (1978) 371–374.
[21] T. Hughes, K. Pister, R. Taylor, Implicit-explicit finite elements in nonlinear transient analysis, Comput. Methods Appl. Mech. Eng. 17/18 (1979) 159–182.
[22] J. Izaguirre, Q. Ma, T. Matthey, J. Willcock, T. Slabach, B. Moore, G. Viamontes, Overcoming instabilities in Verlet-I/r-RESPA with the mollified impulse method, in: T. Schlick, H. Gan (Eds.), Computational Methods for Macromolecules: Challenges and Applications, Proceedings of the Third International Workshop on Algorithms for Macromolecular Modeling, Springer Verlag, 2000.
[23] J. Izaguirre, S. Reich, R. Skeel, Longer time steps for molecular dynamics, J. Chem. Phys. 110 (20) (1999) 9853–9864.
[24] C. Kane, J. Marsden, M. Ortiz, M. West, Variational integrators and the Newmark algorithm for conservative and dissipative mechanical systems, Int. J. Numer. Methods Eng. 49 (10) (2000) 1295–1325.
[25] B. Leimkuhler, S. Reich, Simulating Hamiltonian Dynamics, Cambridge Monographs on Applied and Computational Mathematics, Cambridge University Press, 2005.
[26] A. Lew, Variational time integrators in computational solid mechanics, Ph.D. thesis, Caltech, 2003.
[27] A. Lew, J. Marsden, M. Ortiz, M. West, Asynchronous variational integrators, Arch. Ration. Mech. Anal. 167 (2) (2003) 85–146.
[28] A. Lew, J. Marsden, M. Ortiz, M. West, Variational time integrators, Int. J. Numer. Methods Eng. 60 (2004) 153–212.
[29] A. Lew, M. Ortiz, Asynchronous Variational Integrators in Geometry, Mechanics and Dynamics, Volume dedicated to J. Marsden in his 60th birthday, Springer, 2002.
[30] R. MacKay, Some aspects of the dynamics of Hamiltonian systems, in: D. Broomhead, A. Iserles (Eds.), The Dynamics of Numerics and the Numerics of Dynamics, Clarendon Press, Oxford, 1992, pp. 137–193.
[31] M. Mandziuk, T. Schlick, Resonance in the dynamics of chemical systems simulated by the implicit-midpoint scheme, Chem. Phys. Lett. 237 (1995) 525.
[32] J. Marsden, S. Pekarsky, S. Shkoller, M. West, Variational methods, multisymplectic geometry and continuum mechanics, J. Geomet. Phys. 38 (2001) 253–284.
[33] J. Marsden, M. West, Discrete mechanics and variational integrators, Acta Numer. (2001) 357–514.
[34] T. Miller III, M. Eleftheriou, P. Pattnaik, A. Ndirango, G. Martyna, Symplectic quaternion scheme for biophysical molecular dynamics, J. Chem. Phys. 116 (2002) 8649.
[35] P. Minary, M. Tuckerman, G. Martyna, Long time molecular dynamics for enhanced conformational sampling in biomolecular systems, Phys. Rev. Lett. 93 (2004) 150201.
[36] S. Müller, M. Ortiz, On the gamma-convergence of discrete dynamics and variational integrators, J. Nonlinear Sci. 14 (2004) 279–296.
[37] M. Neal, T. Belytschko, Explicit-explicit subcycling with non-integer time step ratios for structural dynamic systems, Comput. Struct. 6 (1989) 871–880.
[38] S. Reich, Backward error analysis for numerical integrators, SIAM J. Numer. Anal. 36 (5) (1999) 1549–1570.
[39] A. Sandu, T. Schlick, Masking resonance artifacts in force-splitting methods for biomolecular simulations by extrapolative Langevin dynamics, J. Comp. Phys. 151 (1999) 74–113.
[40] J.M. Sanz-Serna, Symplectic integrators for Hamiltonian problems – an overview, Acta Numer. (1992) 243–286.
[41] T. Schlick, M. Mandziuk, R. Skeel, K. Srinivas, Nonlinear resonance artifacts in molecular dynamics simulations, J. Comput. Phys. 139 (1998) 1.
[42] R. Skeel, K. Srinivas, Nonlinear stability analysis of area-preserving integrators, SIAM J. Numer. Anal. 38 (1) (2000) 129–148.
[43] R. Skeel, G. Zhang, T. Schlick, A family of symplectic integrators stability, accuracy, and molecular dynamics applications, SIAM J. Sci. Comput. 18 (1) (1997) 203–222.
[44] R.D. Skeel, K. Srinivas, Nonlinear stability analysis of area-preserving integrators, SIAM J. Numer. Anal. 38 (1) (2000) 129–148.
[45] P. Smolinski, Y.-S. Wu, An implicit multi-time step integration method for structural dynamics problems, Comput. Mech. 22 (1998) 337–343.
[46] Y. Suris, Hamiltonian methods of Runge–Kutta type and their variational interpretation, Math. Model. 2 (1990) 78–87.
[47] M. Tuckerman, B. Berne, G. Martyna, Reversible multiple time scale molecular dynamics, J. Chem. Phys. 97 (1992) 1990–2001.
[48] J.M. Wendlandt, J.E. Marsden, Mechanical integrators derived from a discrete variational principle, Physica D 106 (1997) 223–246.
[49] M. West, Variational integrators, Ph.D. thesis, Caltech, 2004.